



**HAL**  
open science

## A two-step fluid–structure approach for the vibration analysis of flexible propeller blade

Quentin Rakotomalala, Lucie Rouleau, Cédric Leblond, Mickaël Abbas,  
Jean-François Deü

► **To cite this version:**

Quentin Rakotomalala, Lucie Rouleau, Cédric Leblond, Mickaël Abbas, Jean-François Deü. A two-step fluid–structure approach for the vibration analysis of flexible propeller blade. *Journal of Fluids and Structures*, 2024, 126, 10.1016/j.jfluidstructs.2024.104091 . hal-04524594

**HAL Id: hal-04524594**

**<https://hal.science/hal-04524594>**

Submitted on 28 Mar 2024

**HAL** is a multi-disciplinary open access archive for the deposit and dissemination of scientific research documents, whether they are published or not. The documents may come from teaching and research institutions in France or abroad, or from public or private research centers.

L'archive ouverte pluridisciplinaire **HAL**, est destinée au dépôt et à la diffusion de documents scientifiques de niveau recherche, publiés ou non, émanant des établissements d'enseignement et de recherche français ou étrangers, des laboratoires publics ou privés.



# A two-step fluid–structure approach for the vibration analysis of flexible propeller blade

Quentin Rakotomalala<sup>a,b,\*</sup>, Lucie Rouleau<sup>b</sup>, Cédric Leblond<sup>a</sup>, Mickaël Abbas<sup>c</sup>, Jean-François Deü<sup>b</sup>

<sup>a</sup> Centre d'Expertise des Structures et MATériaux Navals (CESMAN) Naval Group, 5 rue de l'halbrane, 44330 Bouguenais, France

<sup>b</sup> Laboratoire de Mécanique des Structures et des Systèmes Couplés (LMSSC) Conservatoire national des arts et métiers (Cnam), 292 rue Saint-Martin, 75141 Paris cedex3, France

<sup>c</sup> Electrotechnique et Mécanique des Structures (ERMES) Department, R&D Division, Electricité de France (EDF), 7 boulevard Gaspard Monge, 91120 Palaiseau, France

## ARTICLE INFO

### Keywords:

Fluid–structure interaction  
Large deformation  
Pre-stressed state  
Vibroacoustic  
Blade element method  
Finite element method

## ABSTRACT

In this paper, a numerical approach able to evaluate the sound power emitted by a non-cavitating flexible marine propeller blade is proposed. With asymptotic expansions and order of magnitude analysis, two main phenomena are identified: the so-called propulsion and vibroacoustic phenomenon. The propulsion phenomenon is nonlinear and models the lift generation along the blade. It creates a pre-stress and a pre-strain on a deformed configuration on which the blade vibrates and emits sound waves. The vibroacoustic phenomenon is linearized and has no retroaction on the first static phenomenon. This simplified model allows to solve the fully coupled fluid–structure system in order to compute the radiated noise of a pre-stressed blade.

## 1. Introduction

In 2004, the International Maritime Organization (IMO) expressed a concern on the effect of underwater anthropogenic noises on the maritime environment and its fauna. In 2014, the IMO released a statement affirming that ship's noise can and should be mitigated. Stealth is also a major design challenge for today's warship, low level of radiated noise ensures a strategic advantage in combat. Hydrodynamic noise derived from flow induced vibrations of propeller blades is one of the phenomenon that must be mitigated in order to achieve a sufficient level of stealthiness (Smith and Rigby, 2022).

In this paper, a numerical approach able to evaluate the sound power emitted by a non-cavitating flexible marine propeller blade is proposed. These vibrations can come from the machinery or hydrodynamic pressure fluctuations especially at high speed revolutions per minute. The turbulent boundary layer imposes a fluctuating pressure on the wetted surface of the blade (Goody, 2004) and may cause annoying vibrations of the structure. These vibrations are then transmitted back to the fluid as sound waves which can be detected by marine wildlife and sonars. Visco-elastic films are able to transform vibration energy into heat thus, they considerably reduce the radiated noise level of underwater structures (see for example Rouleau et al. (2018, 2012) and Leblond and Sigrist (2016)). These materials' characteristics depend on their state of pre-strain and pre-stress. Therefore, in order to compute with

\* Corresponding author at: Laboratoire de Mécanique des Structures et des Systèmes Couplés (LMSSC) Conservatoire national des arts et métiers (Cnam), 292 rue Saint-Martin, 75141 Paris cedex3, France.

E-mail address: [quentin.rakotomalala@orange.fr](mailto:quentin.rakotomalala@orange.fr) (Q. Rakotomalala).

<https://doi.org/10.1016/j.jfluidstructs.2024.104091>

Received 8 May 2023; Received in revised form 16 February 2024; Accepted 21 February 2024

Available online 19 March 2024

0889-9746/© 2024 The Authors. Published by Elsevier Ltd. This is an open access article under the CC BY-NC-ND license (<http://creativecommons.org/licenses/by-nc-nd/4.0/>).

## Nomenclature

### Solid and Fluid

$C_0$	Initial configuration
$C_1$	Intermediate configuration
$C_2$	Actual configuration
$F_{20}$	Gradient of mapping $\phi_{20}$
$F_{10}$	Gradient of mapping $\phi_{10}$
$F_{21}$	Gradient of mapping $\phi_{21}$
$J_{20}$	Jacobian of $F_{20}$
$J_{10}$	Jacobian of $F_{10}$
$J_{21}$	Jacobian of $F_{21}$
$n_0$	Wet surface normal on configuration $C_0$
$n_1$	Wet surface normal on configuration $C_1$
$n_2$	Wet surface normal on configuration $C_2$
$p$	Fluid pressure
$p_1$	Propulsion part of the fluid pressure
$p_2$	Vibroacoustic part of the fluid pressure
$S$	Piola–Kirchhoff II tensor
$x_0$	Solid position in configuration $C_0$
$x_1$	Solid position in configuration $C_1$
$x_2$	Solid position in configuration $C_2$
$\rho^f$	Density of the fluid
$\rho$	Propulsion part of the density of the fluid
$\rho_2$	Vibroacoustic part of the density of the fluid
$\sigma^f$	Fluid stress tensor
$\sigma_1^f$	Propulsion part of the fluid stress tensor
$\sigma_2^f$	Vibroacoustic part of the fluid stress tensor
$\sigma^s$	Solid stress tensor
$\sigma_1^s$	Propulsion part of the solid stress tensor
$\sigma_2^s$	Vibroacoustic part of the solid stress tensor

### Order of magnitudes

$L$	Length of the blade
$p_{acc}$	Order of magnitude of the vibroacoustic pressure
$p_{prop}$	Order of magnitude of the propulsion pressure
$G$	Shear modulus of the blade's material
$\rho^s$	Density of the solid
$v_\infty$	Incident velocity field
$\omega$	Vibration pulsation
$\omega_p$	Angular velocity of the propeller

sufficient accuracy the radiated noise of a damped, rotating propeller blade, there is a need for a specific fluid–structure approach. This approach needs to take into account:

1. lift generation
2. nonlinear pre-stress and pre-strain of the lifting surface
3. linear vibration of the structure
4. added mass and added rigidity of the water to the structure
5. noise propagation in the fluid

The turbulence, cavitation and flow induced noises are not in the scope of this work. However, such phenomena can generate important noise emissions and would therefore need specific studies. The aim of this paper is developing a model that could also be used in an industrial environment. The considered marine propeller is used in a specific regime:

- to avoid cavitation, the velocity at blade tip is limited:  $L\omega_p \lesssim 40 \text{ m s}^{-1}$
- the incident velocity  $v_\infty$ , which is linked to the vessel's speed is of the order of  $10 \text{ m s}^{-1}$
- the frequency of vibration ranges within  $[100, 5000] \text{ Hz}$

The literature covers fully coupled approaches that take into account both the fluid induced deformation and the noise emission of the deformed solid in air, the main applications are airplane's lifting surfaces and helicopter's blade. However, the noise computation of marine structures deals with different physical phenomena and different regimes, the Mach number of the incident flow is very small compared to one. In Choi et al. (2022), a *Reynold Average Navier–Stokes* (RANS) with  $k-\omega$  turbulence model (Wilcox, 2008) fluid solver is coupled to a *Finite Element Method* (FEM) elastic solver. The noise field is computed using a Ffowcs Williams and Hawkings (FW-H) formulation (Testa et al., 2018) coupled to a FEM model of the propeller. As the structure is considered elastic and linear regarding geometry, this approach cannot take into account the pre-strain generated by material nonlinearity. In most work, a choice is made between studying the non linear large deformation fluid–structure interaction and studying small structural vibrations in a weakly compressible fluid. Both phenomena are rarely studied as a whole.

The literature on fluid–structure interaction problem of lifting surfaces in incompressible flow is well furnished and is an active area of research. Many approaches co-exist with different objectives. Depending on the quantity of interest (pressure field, structural criteria, etc.), the effort might be put on the fluid model or on the solid model. In George and Ducoin (2021), the *Direct Numerical Simulation* (DNS) method is used to solve the incompressible fluid flow around a non rotating foil. The foil is simply modeled as a single degree of freedom equation. In this work, many fluid phenomena ranging from lift generation to turbulence can be computed. However, not much can be said about the foil's physics, the flow being considered incompressible, the noise radiation cannot be computed. In Pernod et al. (2017) an *Unsteady Reynolds Averaged Navier–Stokes* (URANS) turbulence model is used coupled to a nonlinear FEM. Both the fluid and structural solvers need to be coupled using *Arbitrary Lagrangian Eulerian* (ALE) method (Hirt et al., 1974). In this work as well, as the fluid is incompressible, the noise radiation cannot be computed using this method. However, it allows to acquire deep insight into both the flow (lift generation and turbulence) and the reaction of the structure. In the work (Lin and Lin, 1996), a *Vortex Lattice Method* (VLM) is coupled to nonlinear FEM. The structure is modeled by 3D shells. The VLM models the flow around a wing or a blade using a square vortex and horseshoe vortex distribution on the camber surface. It is therefore easy to couple with shell elements which also describe the camber surface. In Kim et al. (2021), a VLM is also coupled to nonlinear FEM. Here, 20 nodes hexahedral elements are used. These elements allow to compute more complex stresses criterion. However, a projection operation must be carried out to transfer the 2D pressure field from the VLM to the 3D FEM mesh. In Young (2008), the authors used a 3D *Boundary Element Method* (BEM) coupled with finite element method. The BEM uses the wetted surface mesh which simplifies the projection operation of the pressure field on the FEM mesh. These three approaches focus on the lift induced load and its effect on the structure. Once again, the flow being incompressible and therefore the speed of sound being infinite, it is not possible to directly compute the radiated noise. There is at least two solutions for this problem: the sound propagation could be taken into account by modeling a compressible fluid which has a finite speed of sound and therefore can model propagation phenomenon. The other approach is to model separately the noise propagation with another model. In the case of underwater blades, the speed of sound is much higher than the incident flow velocity. This leads to numerical difficulties as the solver has to accurately represent phenomena with very different orders of magnitude. That is why a separated approach will be considered in this manuscript.

In Hoareau et al. (2022) small vibrations of a structure in contact with a fluid are decoupled from a static pre-stressed state using an asymptotic expansion. The fluid is considered incompressible and therefore the radiated noise cannot be computed from the model. However, the model is able to take into account the effect of a nonlinear pre-stress and a pre-strain on small linear vibrations.

The interaction between a vibrating elastic structure and an acoustic fluid at rest can be tackled by monolithic formulation as described in Morand and Ohayon (1995), Sigrist (2015, 2022), Leblond (2022) and Meyer and Maxit (2022). The  $u-\psi$  formulation of Everstine (1981) uses a velocity potential for the description of the fluid domain and the displacement in the structural domain, it has the advantages of leading to a symmetric matrix formulation without the need for an extra degree of freedom in the fluid, it leads to smaller matrices. This approach models the fluid as an inviscid, linear, potential and weakly compressible acoustic fluid. The structural vibrations are considered small and the problem can be considered linear. The fluid and structure equations are naturally coupled at the wetted surface by boundary conditions. The pre-stress and pre-strain of the structure are not taken into account.

Therefore some approaches are able to compute the nonlinear fluid–structure interaction between a lifting surface and an incompressible flow. Because compressibility of the fluid is ignored in these approaches, they cannot compute noise related quantities. Other approach allows to computation of the radiated noise through a vibroacoustic linear framework that does not take into account the pre-stress or pre strain of the structure. To avoid costly design iteration between blade thrust performance and blade stealthiness, a unified method could be used. In the case of marine propeller, the high speed of sound makes the computation of both sound emission and lift generation by a unique general solver complex from the numerical point of view. There is a huge range of order of magnitude that needs to be covered. In this paper, a simplified two step approach able to take into account both the large transformation induced by lifting flows and noise propagation of the deformed blade is proposed. This simplified methodology can be applied in an industrial context and does not need to engage in specific numerical development in existing tools, the solvers are used as black boxes and features existing in most codes are used. With asymptotic expansions and dimensional analysis, two main phenomena influencing the radiated noise level are identified and partially uncoupled, (i) the fluid–structure interaction associated to the nonlinear large structural displacement and lift induction and (ii) the vibroacoustic problem linearized at this previous state of deformation.

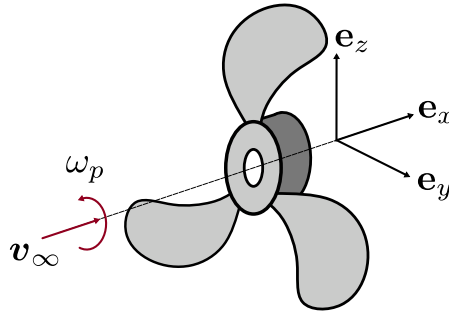


Fig. 1. Rotating propellers axis of references.

## 2. Phenomena separation

In this paper, we will consider a rotating propeller with a constant rotation speed  $\omega_p$  around a fixed axis  $e_x$ , the incident velocity is uniform and will be noted  $v_\infty$  (see Fig. 1). The coupled fluid–structure interaction equations are written in the rotating frame and read:

- Low mach approximation of the compressible Navier–Stokes equations of an isentropic fluid written in Eulerian formulation, for each  $x \in \Omega^f$ :

$$\begin{cases} \partial_t \rho^f \mathbf{v} + \nabla \cdot (\rho^f \mathbf{v} \otimes \mathbf{v}) + 2\rho^f \omega_p \mathbf{R} \mathbf{v} + \rho^f (\omega_p \mathbf{R})^2 \mathbf{x} = \nabla \cdot \boldsymbol{\sigma}^f & \text{(a)} \\ \partial_t \rho^f + \nabla \cdot (\rho^f \mathbf{v}) = 0 & \text{(b)} \\ \rho^f = f(p) & \text{(c)} \end{cases} \quad (1)$$

with  $\mathbf{v}$ ,  $\boldsymbol{\sigma}^f$ ,  $p$  and  $\rho^f$  representing respectively the fluid velocity, stress, pressure and density. The matrix  $\mathbf{R}$  is the linear rotation operator:  $\mathbf{x} \mapsto e_z \wedge \mathbf{x}$ . The constant rotation speed adds two pseudo-forces: a centrifugal force  $(\omega_p \mathbf{R})^2 \mathbf{x}$  and a Coriolis force  $2\omega_p \mathbf{R} \mathbf{v}$ . Eq. (1)a is the conservation of momentum, Eq. (1)b is the continuity equation and Eq. (1)c is the isentropic equation of state of the fluid.

- nonlinear structural equation written on the actual configuration, for each  $\mathbf{x} \in \Omega^s$  :

$$\rho^s \left( \partial_t^2 \mathbf{u} + 2\omega_p \mathbf{R} \partial_t \mathbf{u} + (\omega_p \mathbf{R})^2 \mathbf{x} \right) = \nabla \cdot \boldsymbol{\sigma}^s \quad (2)$$

with  $\mathbf{u}$  and  $\boldsymbol{\sigma}^s$  representing respectively the displacement and the stress. With no translation of the rotation axis and constant rotation velocity, two pseudo-forces arise: a Coriolis force  $2\omega_p \mathbf{R} \partial_t \mathbf{u}$  and a centrifugal force  $(\omega_p \mathbf{R})^2 \mathbf{x}$ .

- These equations are coupled by the boundary conditions:

$$\begin{cases} \boldsymbol{\sigma}^s \mathbf{n} = \boldsymbol{\sigma}^f \mathbf{n} \text{ on } \partial\Omega^s & \text{(a)} \\ \partial_t \mathbf{u} = \mathbf{v} \text{ on } \partial\Omega^s & \text{(b)} \end{cases} \quad (3)$$

where  $\mathbf{n}$  is the outwards normal vector of the structure's wetted surface. Eq. (3)a represents the continuity of the normal stress, Eq. (3)b is the no-slip condition of the fluid. The incident flow  $v_\infty$  in the non rotating frame is homogeneous and constant (see Fig. 1).

The computation of radiated noises can be split into two main phenomena that can be partially uncoupled. The first phenomenon will be called the *propulsive phenomenon*, it is responsible for the lift generation on each blade and the propulsion of the ship. In a general setting, the displacement of the structure can be important (Taketani et al., 2013; Muller and Pécot, 2017) and a nonlinear structure model is required. The velocity of the fluid is of the order of  $v_\infty$  therefore the fluid is low Mach and can be considered incompressible. The second phenomenon is called *vibroacoustic phenomenon*, it takes into account small vibrations of the pre-stress and pre-strain structure. These vibrations generate pressure waves of small amplitudes into the fluid, this phenomenon can be considered linear.

### 2.1. Configurations of the blade

As the structural equation is nonlinear and written in Lagrangian formulation, the notion of configuration becomes of utmost importance. The structural domain  $\Omega_s$  evolves with the application of mechanical loads and boundary conditions. The transformation is described relative to a given reference domain  $C_0$ , usually this reference configuration is the state of the solid at rest. At a given time  $t$ , every point  $\mathbf{x}_0 \in C_0$  in the structural domain suffers a transformation through a bijection  $\phi(\mathbf{x}_0, t)$ , this bijection defines an associated transformed configuration. As displayed in Fig. 2, 3 configurations are considered in this work:

- The initial configuration  $C_0$ , which is the reference configuration.

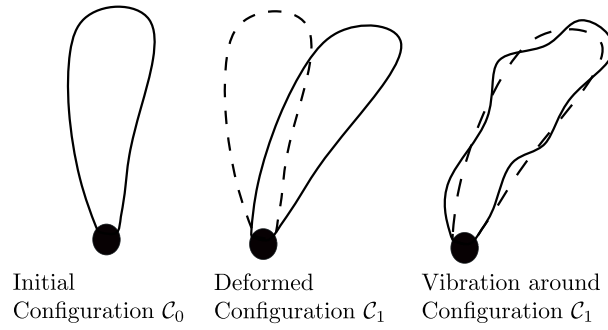


Fig. 2. The three configurations (initial, intermediate and actual) of the propeller.

- The deformed configuration  $C_1$ , which is an intermediate configuration represents the deformed blade resulting from the lift generation.
- The actual configuration  $C_2$ , which is the actual configuration that takes into account both the deformation of the blade resulting from lift generation and the deformation resulting from the blade vibrations.

Operators ( $\nabla \cdot$ ,  $\nabla$ , etc...) written on configuration 0 (respectively 1, 2) will be indexed 0 (respectively 0, 2). The bijections between each configuration read:

- $\mathbf{x}_1 = \phi_{10}(\mathbf{x}_0, t)$  the bijection between the initial configuration  $C_0$  and the configuration  $C_1$ . The displacement therefore reads  $\mathbf{u}_1 = \mathbf{x}_1 - \mathbf{x}_0$ . Its gradient reads  $\mathbf{F}_{10} = \text{Id} + \nabla_0 \mathbf{u}_1$ , and its Jacobian determinant is written  $J_{10}$ .
- $\mathbf{x}_2 = \phi_{21}(\mathbf{x}_1, t)$  the bijection between the configuration  $C_1$  and the actual configuration. The displacement therefore reads  $\mathbf{u}_2 = \mathbf{x}_2 - \mathbf{x}_1$ . Its gradient reads  $\mathbf{F}_{21} = \text{Id} + \nabla_1 \mathbf{u}_2$  and its Jacobian determinant is written  $J_{21}$ .
- $\mathbf{x}_2 = \phi_{20}(\mathbf{x}_0, t)$  the bijection between the initial configuration  $C_0$  and the current configuration  $C_2$ . The displacement therefore reads  $\mathbf{u}_2 = \mathbf{x}_2 - \mathbf{x}_0 = \mathbf{u}_1 + \mathbf{u}_2$ . Its gradient reads  $\mathbf{F}_{20} = \text{Id} + \nabla_0 \mathbf{u}_2 = \mathbf{F}_{21} \mathbf{F}_{10}$  and its Jacobian determinant is written  $J_{20} = J_{21} J_{10}$ .

## 2.2. Examination of the orders of magnitudes of each terms

The marine propeller is considered to operate under the following regime:

- The length of the blade  $L$  is over 1 m.
- To avoid cavitation, the velocity at blade tip is limited:  $L\omega_p \lesssim 40 \text{ m s}^{-1}$  where the propeller rotation speed  $\omega_p$  is considered constant.
- The incident velocity  $v_\infty$ , which is linked to the vessel's speed is of the order of 10  $\text{m s}^{-1}$ , it is also considered constant.
- The speed of sound in the water is  $c = 1500 \text{ m/s}$ , and the reference density is  $\rho = 1000 \text{ kg/m}^3$ .
- The frequency of vibration ranges within [100 Hz, 5 kHz], therefore the associated angular frequency  $2\pi f \gg \omega_p$ .

The fluid pressure field can be split into two contributions. A pressure field contribution  $p_1$  associated to the propulsion phenomenon and linked to the lift generation, it is of the order of magnitude  $p_{prop} = \rho v_\infty^2 \sim 10^5 \text{ Pa}$ . A pressure field contribution  $p_2$  associated to the vibro-acoustic phenomenon and linked to the underwater noise radiation which is of the order of magnitude  $p_{acc} \sim 100 \text{ Pa}$  for a 160 dB noise power. Each quantity (solid displacement, fluid velocity, strain, etc.) is split into two contributions (a propulsion contribution, written with index 1 and vibroacoustic contribution, written with index 2). They are written in non-dimensional form:  $\tilde{X}$  represents the non-dimensional form of quantity  $X$ .

*Time scales in the fluid.* The time scales in the fluid of each phenomenon is also different: the propulsion phenomenon is assumed to have a time scale  $t_1$  equal to  $L/v_\infty$  and the propulsion phenomenon is assumed to have a time scale  $t_2$  equal to  $L/c$ . In the considered regime,  $t_2 \sim 10^{-3} \text{ s}$  and  $t_1 \sim 0.1$ , as there is two order of magnitude between these two time scales, for each quantity  $X$  of the fluid the time derivative operators is split as follow:  $\partial_t X = v_\infty/L_0 \partial_{\tilde{t}_1} X_1 + c/L \partial_{\tilde{t}_2} X_2$ . The non-dimensional form is obtain by dividing by  $v_\infty/L$  :

$$\partial_{\tilde{t}} X = \partial_{\tilde{t}_1} X_1 + \frac{1}{\mathcal{M}} \partial_{\tilde{t}_2} X_2$$

where  $\mathcal{M} = v_\infty/c$  is the mach number of the flow.

*Time scales in the solid.* No assumption is made on the time scale of the solid in the propulsion phenomenon, the time scale of the vibroacoustic phenomenon is  $1/\omega$ .

**Fluid stress.** The fluid stress is assumed to be of the order of magnitude of the pressure fields:  $\sigma^f = p_{prop}\bar{\sigma}_1^f + p_{acc}\bar{\sigma}_2^f$ , the fluid stress is then divided by  $p_{prop}$  to get a non-dimensional form:

$$\bar{\sigma}^f = \bar{\sigma}_1^f + \eta\bar{\sigma}_2^f \quad (4)$$

where  $\eta = p_{acc}/p_{prop}$  is the ratio of order of magnitude between the propulsion and vibroacoustic pressure fields.

**Fluid velocity.** The propulsion fluid velocity's order of magnitude is assumed to be equal to  $v_\infty$ . The equation of a linear acoustic fluid is  $\rho\partial_t v = -\nabla p$  therefore the acceleration field in the acoustic wave propagation is related to the pressure gradient, that is why the vibro-acoustic phenomenon velocity field order of magnitude is assumed to be equal to  $p_{acc}/(\rho c)$ . Therefore  $v = v_\infty\bar{v}_1 + p_{acc}/(\rho c)\bar{v}_2$ . The velocity field is therefore divided by  $v_\infty$  to get the non-dimensional form:

$$\begin{aligned} \bar{v} &= \bar{v}_1 + \frac{p_{acc}}{\rho c v_\infty}\bar{v}_2 \\ &= \bar{v}_1 + \eta\mathcal{M}\bar{v}_2 \end{aligned}$$

**Fluid density.** The propulsion fluid density is assumed to be constant and equal to  $\rho$  the reference fluid density, the propulsion phenomenon is assumed to be incompressible. An asymptotic expansion of the equation of state (1)c is performed around  $p_1$ :  $\rho^f = f(p_1) + \partial_p f(p_1)p_2$ . The derivative  $\partial_p f(p_1)$  is the square of the sound celerity in the fluid  $c^2$ , the order of magnitude of the vibroacoustic density is therefore assumed to be equal to  $p_{acc}/c^2$ . Therefore  $\rho^f = \rho + p_{acc}/c^2\bar{\rho}_2$ , the fluid density is divided by  $\rho$  to get the non-dimensional form:

$$\begin{aligned} \bar{\rho}^f &= 1 + \frac{p_{acc}}{\rho c^2}\bar{\rho}_2 \\ &= 1 + \eta\mathcal{M}^2\bar{\rho}_2 \end{aligned}$$

**Structural displacement.** The structural displacement part of the propulsion phenomenon is the result of an equilibrium between the fluid pressure field and the deformable solid stiffness, it is assumed that the blade will mainly suffer a bending motion, therefore the order of magnitude of the propulsion phenomenon displacement field is  $p_{prop}L/G$  where  $G$  is the shear modulus of the blade's material. As there is a continuity of the velocity field between the fluid and the solid, the order of magnitude of the displacement field of the vibroacoustic phenomenon is  $p_{acc}/(\rho L\omega c)$ . Therefore  $u = p_{prop}L/G\bar{u}_1 + p_{acc}/(\rho L\omega c)\bar{u}_2$ , the displacement field is divided by  $p_{prop}L/G$  to get the non-dimensional

$$\begin{aligned} \bar{u} &= \bar{u}_1 + \frac{p_{acc}}{p_{prop}}\frac{G}{\rho(L\omega)c}\bar{u}_2 \\ &= \bar{u}_1 + \eta\mathcal{G}\mathcal{V}\mathcal{M}\bar{u}_2 \end{aligned}$$

where  $\mathcal{G} = \frac{G}{\rho v_\infty^2}$  is the ratio bending modulus to incident pressure field and  $\mathcal{V} = \frac{v_\infty}{L\omega}$ .

### 2.3. Equation of the structure

The structural equations of the propulsion phenomenon on one hand and of the vibroacoustic phenomenon on the other hand are determined in this subsection. First Equation (2) is written on the initial configuration, that way the divergence operator is written on the configuration  $C_0$  and all geometrical variations are taken into account in the appropriate stress tensor, it reads:

$$\rho_s \left( \partial_t^2 \mathbf{u} + 2\omega_p \mathbf{R} \partial_t \mathbf{u} + (\omega_p \mathbf{R})^2 \mathbf{x} \right) = \nabla_0 \cdot \mathbf{P}(\mathbf{u}) \quad (5)$$

where  $\mathbf{P}$  is the Piola–Kirchhoff I (PK I) tensor, it represents stress of the current configuration projected on the initial configuration, it is linked to the Cauchy stress tensor using relation  $\mathbf{P} = J_{20}^{-1} \sigma^s F_{20}^T$ . Because a majority of the constitutive laws are written in terms of Piola–Kirchhoff II (PK II) tensor  $\mathcal{S}$ , and in finite element method, the interior force vector operator is written as a function of tensor  $\mathcal{S}$ . Therefore it is convenient to rewrite PK I tensor as a function of PK II using the relation  $\mathbf{P}(\mathbf{u}) = F_{20}(\mathbf{u})\mathcal{S}(\mathbf{u})$ . Recall from paragraph 2.2 that  $\|\mathbf{u}_2\|/\|\mathbf{u}_1\| \sim \eta\mathcal{G}\mathcal{V}\mathcal{M}$ , in the specific regime  $\eta\mathcal{G}\mathcal{V}\mathcal{M} = 10^{-3}$ , then  $\mathbf{u}_2$  has a order of magnitude much smaller than  $\mathbf{u}_1$  and a linearization is legitimate. Let  $\mathbf{u} = \mathbf{u}_1 + \mu\bar{\mathbf{u}}_2$ , where  $\mu = \eta\mathcal{G}\mathcal{V}\mathcal{M}p_{prop}L/G$  is the order of magnitude of  $\mathbf{u}_2$  relative to  $\mathbf{u}_1$ , the asymptotic expansion is carried out following the steps:

- The Piola–Kirchhoff II tensor can be linearized in  $\mu$ :  $\mathcal{S}(\mathbf{u}) = \mathcal{S}(\mathbf{u}_1) + \mu d\mathcal{S}_{u_1}(\bar{\mathbf{u}}_2) + \mathcal{O}(\mu^2)$  where  $d\mathcal{S}_{u_1}$  is the differential of  $\mathcal{S}$  at point  $\mathbf{u}_1$ . The Piola–Kirchhoff I can therefore be expanded as follows:

$$\begin{aligned} \mathbf{P}(\mathbf{u}) &= F_1(\mathbf{u}_2)F_0(\mathbf{u}_1)\mathcal{S}(\mathbf{u}_1 + \mu\bar{\mathbf{u}}_2) \\ &= [\text{Id} + \mu\nabla_1\bar{\mathbf{u}}_2]F_0 \left[ \mathcal{S}(\mathbf{u}_1) + \mu d\mathcal{S}_{u_1}(\bar{\mathbf{u}}_2) + \mathcal{O}(\mu^2) \right] \\ &= F_0\mathcal{S}(\mathbf{u}_1) + \mu \left[ F_0 d\mathcal{S}_{u_1}(\bar{\mathbf{u}}_2) + (\nabla_1\bar{\mathbf{u}}_2)F_0\mathcal{S}(\mathbf{u}_1) \right] + \mathcal{O}(\mu^2) \\ &= \mathbf{P}_1 + \mu\bar{\mathbf{P}}_2 + \mathcal{O}(\mu^2) \end{aligned}$$

- The acceleration is expanded as follows:

$$\partial_t^2 \mathbf{u} + 2\omega_p \mathbf{R} \partial_t \mathbf{u} + (\omega_p \mathbf{R})^2 \mathbf{x} = \partial_t^2 \mathbf{u}_1 + 2\omega_p \mathbf{R} \partial_t \mathbf{u}_1 + (\omega_p \mathbf{R})^2 \mathbf{x}_1 + \mu(\partial_t^2 \bar{\mathbf{u}}_2 + 2\omega_p \mathbf{R} \partial_t \bar{\mathbf{u}}_2 + (\omega_p \mathbf{R})^2 \bar{\mathbf{u}}_2)$$

Two sets of equations can therefore be deduced, the terms of order 0 in  $\mu$  give the structural propulsion equation written on configuration  $C_0$ :

$$\rho_s \left( \partial_t^2 \mathbf{u}_1 + 2\omega_p \mathbf{R} \partial_t \mathbf{u}_1 + (\omega_p \mathbf{R})^2 \mathbf{x}_1 \right) = \nabla_0 \cdot \mathbf{P}_1 \quad (6)$$

Using relation  $\sigma_1^s = J_0^{-1} \mathbf{P}_1 \mathbf{F}_0^T$ , Eq. (6) can be written on the intermediate configuration  $C_1$ . The tensor  $\sigma_1^s$  is the Cauchy tensor of the propulsion phenomenon.

$$\rho_s \left( \partial_t^2 \mathbf{u}_1 + 2\omega_p \mathbf{R} \partial_t \mathbf{u}_1 + (\omega_p \mathbf{R})^2 \mathbf{x}_1 \right) = \nabla_1 \cdot \sigma_1^s \quad (7)$$

The terms of order 1 in  $\mu$  gives the vibroacoustic equation. On the initial configuration  $C_0$  it reads:

$$\rho_s \left( \partial_t^2 \mathbf{u}_2 + 2\omega_p \mathbf{R} \partial_t \mathbf{u}_2 + (\omega_p \mathbf{R})^2 \mathbf{u}_2 \right) = \nabla_0 \cdot \mathbf{P}_2 \quad (8)$$

where  $\mathbf{P}_2 = \mu \bar{\mathbf{P}}_2$ , using again relation  $\sigma_2^s = J_0^{-1} \mathbf{P}_2 \mathbf{F}_0^T$ , Eq. (6) can be written on the intermediate configuration  $C_1$  and in the Fourier space, it yields:

$$\rho_s \left( -\omega^2 \mathbf{u}_2 + 2\omega_p \omega i \mathbf{R} \mathbf{u}_2 + (\omega_p \mathbf{R})^2 \mathbf{u}_2 \right) = \nabla_1 \cdot \sigma_2^s \quad (9)$$

As  $\omega \ll \omega_p$  in the considered regime, the inertial forces can be neglected and the equation in the structural domain becomes:

$$-\rho_s \omega^2 \mathbf{u}_2 = \nabla_1 \cdot \sigma_2^s \quad (10)$$

The tensor  $\sigma_2^s$  is a pseudo-Cauchy stress tensor, as it represents the stress of the vibroacoustic phenomenon on the intermediate configuration, it has two contributions namely:

- the material stress which takes into account the phenomenon linked to the constitutive law of the material via the differential of  $\mathcal{S}$  and reads:  $\sigma_2^m = J_0^{-1} \mathbf{F}_0 d\mathcal{S}_{\mathbf{u}_1}(\mathbf{u}_2) \mathbf{F}_0^T$
- the geometrical stress, which factors in the pre-stress of the structure, it reads:  $\sigma_2^g = (\nabla_1 \mathbf{u}_2) \sigma_1(\mathbf{u}_1)$

It is worth noting that the linearized vibroacoustic stress tensor is not symmetric on configuration  $C_1$ . However, in weak form, this stress tensor is associated to the operator  $W_2^{\text{int}}(\mathbf{v}, \mathbf{u}_2) = \int_{\Omega_1} \sigma_2^g(\mathbf{u}_2) : \nabla_1 \mathbf{v}$  which is symmetric (meaning  $\mathbf{v}$  and  $\mathbf{u}_2$  are interchangeable) therefore leading to a symmetric matrix formulation.

## 2.4. Equation of the fluid

The fluid equations for the propulsion and vibroacoustic phenomenon are then determined in this section. First the conservation of momentum (Eq. (1)a) is rewritten in convective form using the conservation of mass (Eq. (1)b), this equation reads:

$$\rho^f \left( \partial_t \mathbf{v} + (\mathbf{v} \cdot \nabla) \mathbf{v} + 2\omega_p \mathbf{R} \mathbf{v} + (\omega_p \mathbf{R})^2 \mathbf{x} \right) = \nabla \cdot \sigma^f \quad (11)$$

It is then written in non-dimensional form using notation from Section 2.2:

$$\bar{\rho} \left( \partial_t \bar{\mathbf{v}} + (\bar{\mathbf{v}} \cdot \nabla) \bar{\mathbf{v}} + \frac{2}{J} \mathbf{R} \bar{\mathbf{v}} + \left( \frac{\mathbf{R}}{J} \right)^2 \left( \bar{\mathbf{x}}_0 + \frac{P_{prop}}{G} \bar{\mathbf{u}} \right) \right) = \bar{\nabla} \cdot \bar{\sigma}^f \quad (12)$$

where  $J = v_\infty / (L_0 \omega_p)$  is the advance ratio. The non-dimensional quantities are then split between a propulsion contribution and a vibroacoustic contribution:

$$\left( \partial_t \bar{\mathbf{v}}_1 + \frac{1}{\mathcal{M}} \partial_{\bar{t}_2} (\eta \mathcal{M} \bar{\mathbf{v}}_2) + ((\bar{\mathbf{v}}_1 + \eta \mathcal{M} \bar{\mathbf{v}}_2) \cdot \nabla) (\bar{\mathbf{v}}_1 + \eta \mathcal{M} \bar{\mathbf{v}}_2) + \frac{2}{J} \mathbf{R} (\bar{\mathbf{v}}_1 + \eta \mathcal{M} \bar{\mathbf{v}}_2) + \left( \frac{\mathbf{R}}{J} \right)^2 \left( \bar{\mathbf{x}}_0 + \frac{P_{prop}}{G} \bar{\mathbf{u}}_1 + \eta \mathcal{M} \mathcal{V} \bar{\mathbf{u}}_2 \right) \right) = \bar{\nabla} \cdot \bar{\sigma}_1^f + \eta \bar{\nabla} \cdot \bar{\sigma}_2^f \quad (13)$$

Recall from Section 2.3 that  $\eta \ll 1$  and as in this regime  $\mathcal{V} \ll 1$  and  $\mathcal{M} \ll 1$ , the propulsion and vibroacoustic are therefore of different order of magnitude. Order 0 in  $\eta$  in Eq. (13) is identified with the equation of momentum balance of the propulsion phenomenon, it reads in dimensional form:

$$\rho \left( \partial_t \mathbf{v}_1 + (\mathbf{v}_1 \cdot \nabla) \mathbf{v}_1 + 2\omega_p \mathbf{R} \mathbf{v}_1 + (\omega_p \mathbf{R})^2 \mathbf{x} \right) = \nabla \cdot \sigma_1^f \quad (14)$$

The vibroacoustic phenomenon is identified with order 1 in  $\eta$ , in non-dimensional form it reads:

$$\left( \partial_{\bar{t}_2} \bar{\mathbf{v}}_2 + \mathcal{M} [(\bar{\mathbf{v}}_1 \cdot \nabla) \bar{\mathbf{v}}_2]^{sym} + \frac{2\mathcal{M}}{J} \mathbf{R} \bar{\mathbf{v}}_2 + \mathcal{M} \mathcal{V} \left( \frac{1}{J} \mathbf{R} \right)^2 \bar{\mathbf{u}}_2 \right) = \bar{\nabla} \cdot \bar{\sigma}_2^f - \mathcal{M}^2 \bar{\rho}_2 \left( \partial_t \bar{\mathbf{v}}_1 + (\bar{\mathbf{v}}_1 \cdot \nabla) \bar{\mathbf{v}}_1 + \frac{2}{J} \mathbf{R} \bar{\mathbf{v}}_1 + \left( \frac{\mathbf{R}}{J} \right)^2 \left( \bar{\mathbf{x}}_0 + \frac{P_{prop}}{G} \bar{\mathbf{u}}_1 \right) \right) \quad (15)$$

where  $[(\bar{\mathbf{v}}_1 \cdot \nabla) \bar{\mathbf{v}}_2]^{sym} = (\bar{\mathbf{v}}_1 \cdot \nabla) \bar{\mathbf{v}}_2 + (\bar{\mathbf{v}}_2 \cdot \nabla) \bar{\mathbf{v}}_1$ . As  $J \sim 1$ ,  $\mathcal{V} \ll 1$  and  $\mathcal{M} \ll 1$ , the vibroacoustic momentum balance can be simplified and reads:

$$\partial_{\bar{t}_2} \bar{\mathbf{v}}_2 = \bar{\nabla} \cdot \bar{\sigma}_2^f \quad (16)$$



In dimensional form, it reads:

$$\rho \partial_t \mathbf{v}_2 = \nabla \cdot \boldsymbol{\sigma}_2^f \quad (17)$$

Note that in the specific regime considered, the forcing terms coming from the propulsion phenomenon flow can be neglected. In low Mach regime, there is no retroaction of the propulsion phenomenon on the sound wave generation.

The continuity equation (Eq. (1)b) is now considered and is written in non-dimensional form:

$$\frac{1}{\mathcal{M}} \partial_{\tilde{t}_2} (\eta \mathcal{M}^2 \tilde{\rho}_2) + \tilde{\nabla} \cdot ((1 + \eta \mathcal{M}^2 \tilde{\rho}_2) (\tilde{\mathbf{v}}_1 + \eta \mathcal{M} \tilde{\mathbf{v}}_2)) = 0 \quad (18)$$

as  $\mathcal{M} \ll 1$  and  $\eta \ll 1$  the propulsion and vibroacoustic phenomenon have different order of magnitudes, therefore the propulsion continuity equation is the order 0 in  $\eta$ , it reads in dimensional form:

$$\nabla \cdot \mathbf{v}_1 = 0 \quad (19)$$

The order 1 in  $\eta$  is identified with the vibroacoustic continuity equation, it reads:

$$\partial_{\tilde{t}_2} \tilde{\rho}_2 + \tilde{\nabla} \cdot (\mathcal{M} \tilde{\rho}_2 \tilde{\mathbf{v}}_1) + \tilde{\nabla} \cdot \tilde{\mathbf{v}}_2 = 0 \quad (20)$$

As  $\mathcal{M} \ll 1$ , this equation can be simplified, it reads in dimensional form:

$$\partial_t \rho_2 + \nabla \cdot \mathbf{v}_2 = 0 \quad (21)$$

## 2.5. Boundary conditions

The boundary condition can also be simplified by expanding each terms in orders of  $\eta$ . The order 0 gives the propulsion contribution and order 1 gives the vibroacoustic contribution. Recall from Eqs. (3)a and (3)b, the two boundary conditions involved in the fluid–structure interaction problem read on the actual configuration  $C_2$ :

- the dynamic condition:  $\boldsymbol{\sigma}^s \mathbf{n}_2 = \boldsymbol{\sigma}^f \mathbf{n}_2$  on  $\partial\Omega^s$ ;
- the kinematic condition:  $\partial_t \mathbf{u} = \mathbf{v}$  on  $\partial\Omega^s$

### 2.5.1. Dynamic condition

In order to take into account the change in geometry, the asymptotic expansion of the dynamic condition must be carried out on the initial configuration  $C_0$ . Normal  $\mathbf{n}_2$  of the wetted surface on the actual configuration  $C_2$  is related to the normal  $\mathbf{n}_0$  of the wetted surface in the initial configuration  $C_0$  in relation  $\mathbf{n}_2 ds_2 = J_{20} \mathbf{F}_{20}^{-T} ds_0$ , where  $ds_2$  (respectively  $ds_0$ ) is an infinitesimal surface element on the actual configuration (respectively the initial configuration). Therefore, the dynamic condition can be written on the initial configuration  $C_0$ . First Equation (3)a is multiplied on both sides by  $ds_2$  it reads:  $\boldsymbol{\sigma}^s \mathbf{n}_2 ds_2 = \boldsymbol{\sigma}^f \mathbf{n}_2 ds_2$ . Then by using relation  $\mathbf{n}_2 ds_2 = J_{20} \mathbf{F}_{20}^{-T} \mathbf{n}_0 ds_0$ , it can be written on the initial configuration, it reads:

$$J_{20} \boldsymbol{\sigma} \mathbf{F}_{20}^{-T} \mathbf{n}_0 ds_0 = J_{20} \boldsymbol{\sigma}^f \mathbf{F}_{20}^{-T} \mathbf{n}_0 ds_0 \quad (22)$$

Using the relation between Piola–Kirchhoff I and the Cauchy tensor:  $\mathbf{P} = J_{20} \boldsymbol{\sigma}^s \mathbf{F}_{20}^{-T} \mathbf{n}_0$ , Eq. (22) can be simplified:

$$\mathbf{P} \mathbf{n}_0 ds_0 = J_{20} \boldsymbol{\sigma}^f \mathbf{F}_{20}^{-T} \mathbf{n}_0 ds_0 \quad (23)$$

Each term of Eq. (23) can be split into a vibroacoustic contribution and propulsion contribution, using the previous sections notations, it reads:

- the Piola–Kirchhoff I tensor:  $\mathbf{P} = p_{prop} (\tilde{\mathbf{P}}_1 + \eta \mathcal{M} \mathcal{V} \tilde{\mathcal{G}} \tilde{\mathbf{P}}_2)$  using the 2.3 PK I decomposition and  $\mathbf{P}$  being assumed to be of the order of  $p_{prop}$ .
- the fluid stress:  $\boldsymbol{\sigma}^f = p_{prop} (\tilde{\boldsymbol{\sigma}}_1^f + \eta \tilde{\boldsymbol{\sigma}}_2^f)$
- the Jacobian determinant:

$$\begin{aligned} J_{20}(\mathbf{u}) &= J_{21}(\mathbf{u}_2) J_{10}(\mathbf{u}_1) \\ &= J_{10}(\mathbf{u}_1) \det(\text{Id} + \eta \mathcal{M} \mathcal{V} \tilde{\nabla}_1 \tilde{\mathbf{u}}_2) \\ &= J_{10}(\mathbf{u}_1) (1 + \eta \mathcal{M} \mathcal{V} \text{Tr}(\tilde{\nabla}_1 \tilde{\mathbf{u}}_2)) + O(\eta^2) \\ &\simeq J_{10}(\mathbf{u}_1) (1 + \eta \mathcal{M} \mathcal{V} \text{Tr}(\tilde{\nabla}_1 \tilde{\mathbf{u}}_2)) \end{aligned}$$

- the gradient tensor term:

$$\begin{aligned} \mathbf{F}_{20}^{-T}(\mathbf{u}) &= (\mathbf{F}_{21}(\mathbf{u}_2) \mathbf{F}_{10}(\mathbf{u}_1))^{-T} \\ &= (\mathbf{F}_{10}(\mathbf{u}_1))^{-T} (\text{Id} + \eta \mathcal{M} \mathcal{V} \nabla_1 \tilde{\mathbf{u}}_2)^{-T} \\ &= (\mathbf{F}_{10}(\mathbf{u}_1))^{-T} (\text{Id} - \eta \mathcal{M} \mathcal{V} (\tilde{\nabla}_1 \tilde{\mathbf{u}}_2)^T) + O(\eta^2) \\ &\simeq (\mathbf{F}_{10}(\mathbf{u}_1))^{-T} (\text{Id} - \eta \mathcal{M} \mathcal{V} (\tilde{\nabla}_1 \tilde{\mathbf{u}}_2)^T) \end{aligned}$$

The dynamic condition in non-dimensional form therefore reads:

$$(\tilde{P}_1 + \eta \mathcal{M}\mathcal{V}\mathcal{G}\tilde{P}_2)\mathbf{n}_0 ds_0 = J_{10} \left( \tilde{\sigma}_1^f (1 + \eta \mathcal{M}\mathcal{V} (\mathbf{Tr}(\tilde{\nabla}_1 \tilde{\mathbf{u}}_2) - F_{10}^{-T} \tilde{\nabla}_1 \tilde{\mathbf{u}}_2 F_{10}^T)) + \eta \tilde{\sigma}_2^f \right) F_{10}^{-T} \mathbf{n}_0 ds_0 \quad (24)$$

In the specific regime considered,  $\eta \ll 1$ ,  $\eta \mathcal{M}\mathcal{V} \ll 1$  and  $\eta \mathcal{M}\mathcal{V}\mathcal{G} \ll 1$ , the propulsion and vibroacoustic phenomenon contributions to the boundary conditions have different order of magnitudes and order 0 in  $\eta$  is identified with the propulsion dynamic condition, in dimensional form it reads:

$$\mathbf{P}_1 \mathbf{n}_0 ds_0 = J_{10} \sigma_1^f F_{10}^{-T} \mathbf{n}_0 ds_0 \quad (25)$$

Using relation  $\mathbf{n}_1 ds_1 = J_{10} F_{10}^{-T} \mathbf{N} ds_0$  that links the normal on configuration  $C_1$  to the normal on configuration  $C_0$ , Eq. (25) reads:  $\sigma_1^s \mathbf{n}_1 ds_1 = \sigma_1^f \mathbf{n}_1 ds_1$ . This relation being true for every infinitesimal surface  $ds_1$ , it can be simplified:

$$\sigma_1^s \mathbf{n}_1 = \sigma_1^f \mathbf{n}_1 \quad (26)$$

The dynamic condition of the vibroacoustic phenomenon is identified with order 1 in  $\eta$ , it reads in non-dimensional form:

$$\mathcal{M}\mathcal{V}\mathcal{G}\tilde{P}_2 \mathbf{n}_0 ds_0 = J_{10} \left( \mathcal{M}\mathcal{V} \tilde{\sigma}_1^f (\mathbf{Tr}(\tilde{\nabla}_1 \tilde{\mathbf{u}}_2) - F_{10}^{-T} \tilde{\nabla}_1 \tilde{\mathbf{u}}_2 F_{10}^T) + \tilde{\sigma}_2^f \right) F_{10}^{-T} \mathbf{n}_0 ds_0 \quad (27)$$

In the considered regime,  $\mathcal{M}\mathcal{V}\mathcal{G} \sim 1$  and  $\mathcal{M}\mathcal{V} \ll 1$ , therefore the boundary condition can be simplified. It reads in dimensional form:

$$\mathbf{P}_2 \mathbf{n}_0 ds_0 = J_{10} \sigma_2^f F_{10}^{-T} \mathbf{n}_0 ds_0 \quad (28)$$

Using again relation  $\mathbf{n}_1 ds_1 = J_{10} F_{10}^{-T} \mathbf{N} ds_0$ , Eq. (28) can be written on configuration  $C_1$  and it reads:  $\sigma_2 \mathbf{n}_1 ds_1 = \sigma_2^f \mathbf{n}_1 ds_1$ , this relation being true for every infinitesimal surface  $ds_1$ , the boundary condition becomes:

$$\sigma_2 \mathbf{n}_1 = \sigma_2^f \mathbf{n}_1 \quad (29)$$

### 2.5.2. Kinematic condition

This condition is linear in  $\mathbf{u}$  and  $\mathbf{v}$  therefore the separation is straightforward:

- the kinematic condition of the propulsion phenomenon reads:

$$\partial_t \mathbf{u}_1 = \mathbf{v}_1 \text{ sur } \partial\Omega^s \quad (30)$$

- and the kinematic condition of the vibroacoustic phenomenon reads:

$$\partial_t \mathbf{u}_2 = \mathbf{v}_2 \text{ sur } \partial\Omega^s \quad (31)$$

## 2.6. Simplified equations

In this section, the problem of a radiating marine propeller was modeled by taking into account two main phenomena:

1. the propulsion phenomenon, which gives the deformed geometry and the pre-stress in the structure
2. the vibroacoustic phenomenon, which models the propagation of sound waves in the fluid due to the vibration of the immersed blade.

These two phenomena are partially decoupled, they can be sequentially solved: the propulsion phenomenon results gives the pre-strain and the pre-stress as input to the vibroacoustic phenomenon's equations. From now on the propulsion phenomenon will be considered stationary in the rotating frame. Moreover, the viscous phenomena are neglected and the fluid stress tensor becomes  $\sigma_1^f = -p_1 \text{Id}$ . Because of this simplification, the propulsion kinematic condition must be simplified to an impermeability condition:  $\langle \partial_t \mathbf{u}_1, \mathbf{n}_1 \rangle = \langle \mathbf{v}_1, \mathbf{n}_1 \rangle$  on  $\partial\Omega^s$ . The full set of equations of the propulsion phenomenon becomes :

$$\left\{ \begin{array}{ll} \rho \left( (\mathbf{v}_1 \cdot \nabla) \mathbf{v}_1 + 2\omega_p \mathbf{R} \mathbf{v}_1 + (\omega_p \mathbf{R})^2 \mathbf{x} \right) & = -\nabla p_1 \quad \text{in } \Omega^f \\ \nabla \cdot \mathbf{v}_1 & = 0 \quad \text{in } \Omega^f \\ \rho_s (\omega_p \mathbf{R})^2 \mathbf{x}_1 & = \nabla_1 \cdot \sigma_1^s \quad \text{in } \Omega^s \\ \sigma_1 \mathbf{n}_1 & = -p_1 \mathbf{n}_1 \quad \text{on } \partial\Omega^s \\ 0 & = \langle \mathbf{v}_1, \mathbf{n}_1 \rangle \quad \text{on } \partial\Omega^s \end{array} \right. \quad (32)$$

The vibroacoustic problem is linear and the velocity of the fluid derives from a potential :  $\mathbf{v}_2 = \nabla \psi_2$  (see [Everstine \(1981\)](#)). The viscous terms are also neglected in the vibroacoustic stress tensor and:  $\sigma_2^f = -p_2 \text{Id}$ , therefore kinematic condition is also simplified to an impermeability condition:  $\langle \partial_t \mathbf{u}_2, \mathbf{n}_2 \rangle = \langle \mathbf{v}_2, \mathbf{n}_2 \rangle$  on  $\partial\Omega^s$ . The structure suffers a surface pressure  $p^{\text{excit}}$  load which originates from the incident flow's turbulence pressure. In the Fourier space, the set of equation of the vibroacoustic phenomenon is:

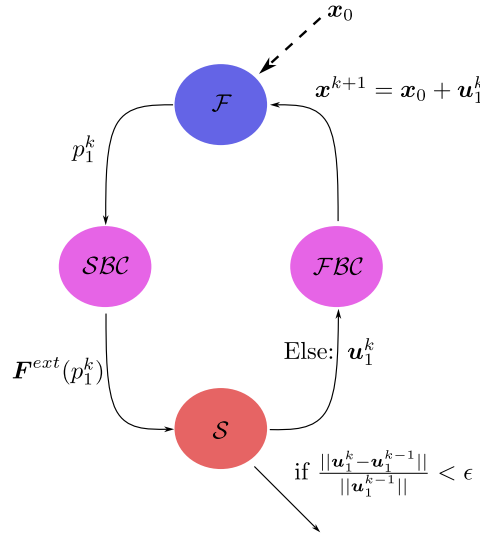


Fig. 3. Iterative Neumann/Neumann algorithm used to couple the fluid solver and structure solver.

$$\left\{ \begin{array}{ll} \rho_s \omega^2 \mathbf{u}_2 + \nabla_1 \cdot \boldsymbol{\sigma}_2 = 0 & \text{in } \Omega^s \\ \left(\frac{e}{c}\right)^2 \psi_2 + \Delta \psi_2 = 0 & \text{in } \Omega^f \\ i\omega \langle \mathbf{u}_2, \mathbf{n} \rangle = \langle \nabla \psi_2, \mathbf{n} \rangle & \text{on } \partial \Omega^s \\ \boldsymbol{\sigma}_2 \mathbf{n} = i\omega \rho_f \psi_2 \mathbf{n} & \text{on } \partial \Omega^s \\ \boldsymbol{\sigma}_2 \mathbf{n} = -p^{\text{excit}} \mathbf{n} & \text{on } \Gamma^{\text{excit}} \end{array} \right. \quad (33)$$

### 3. Solver for the propulsion problem

#### 3.1. Iterative resolution

The fluid/structure equations of the propulsion phenomenon are strongly coupled and nonlinear. Due to the fluid load, the change in geometry between the initial configuration  $C_0$  and the configuration  $C_1$  can be significant. The fluid equations are written on the configuration  $C_1$  and therefore depends on the displacement of the structure which is computed by solving a nonlinear structure problem. Let  $F$  and  $S$  be the fluid and structure solvers,  $(\mathbf{u}_1, p_1)$  the displacement and the fluid pressure, the system of equations to solve can be written in a symbolic manner:

$$\begin{cases} p_1 = F(\mathbf{u}_1) \\ \mathbf{u}_1 = S(p_1) \end{cases} \quad (34)$$

Here  $F$  is related to the first and second equations of the system (32), and  $S$  is related to the third equation of the system (32).

The system (34) is solved using an iterative method described in Fig. 3. This algorithm is used both in Kim et al. (2013) and Kalumuck et al. (1995). In these works the algorithm was used in transient problems, time stepping and numerical damping had to be cautiously tuned. In the steady case under consideration, such aspect need not be taken into account. The solution  $(\mathbf{u}_1, p_1)$  is approached by a sequence  $(\mathbf{u}_1^k, p_1^k)$  defined by:

- $\mathbf{u}_1^0 = 0$
- $p_1^k = F(\mathbf{u}_1^{k-1})$
- $\mathbf{u}_1^k = S(p_1^k)$

The iterations are stopped when the relative error  $\|\mathbf{u}_1^k - \mathbf{u}_1^{k-1}\| / \|\mathbf{u}_1^{k-1}\|$  is smaller than a given error  $\epsilon = 10^{-5}$ . If this sequence is convergent, its limit is solution of the fluid/structure coupled problem. The fluid and structural solvers are coupled by the solid boundary condition (SBC):  $\boldsymbol{\sigma}_1^s \mathbf{n}_1 = -p_1 \mathbf{n}_1$  and the fluid boundary condition (FBC):  $\langle \mathbf{v}_1, \mathbf{n}_1 \rangle = 0$ . This algorithm is non intrusive, the fluid and structure solvers are black box that can be changed at will. However, there is no general proof of convergence and this coupling algorithm is known to fail in some cases. In the specific regime studied, the convergence was achieved using relaxation in a few iteration (less than 15).

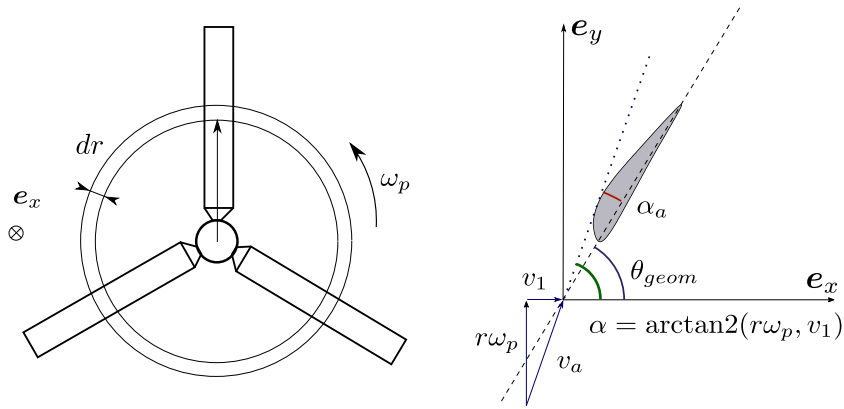


Fig. 4. Schematic defining the notation used in the blade element method.

### 3.2. Fluid solver, blade element method

The fluid equations of the propulsion phenomenon are the incompressible Navier and Stokes equations, the computation of pressure distributions and global forces is well documented and many simplified approach exists. In this study a complete and precise incompressible fluid model is not needed and the blade element method (Glauert, 1935) is used. It is a simplified method used in pre-design studies of propellers. The interaction between blades and the flow around the axis of the blades are deemed negligible. The blades are cut along the radial axis and each blade sections of infinitesimal thickness  $dr$  are considered independent from one another. They are modeled as a 2D section immersed in a 2D flow. The propulsion phenomenon is therefore split into independent bi-dimensional lifting flow computation (see Fig. 4).

The reference axis system of a blade is denoted :  $(e_x, e_y, e_l)$  where  $e_l$  is the direction of the spar and  $e_x$  is the rotation axis. The incident flow generated by the ship motion reads  $v_\infty e_x$  and the rotation speed of the propeller  $\omega_p$  is constant. The bi-dimensional sections are characterized by a chord  $c(r)$ , a rake angle  $\theta_{geom}$  and a pressure coefficient  $C_p$  that needs to be computed.

The section at distance  $r$  from the hub suffers a flow with a velocity norm  $v_a = \sqrt{v_\infty^2 + (\omega_p r)^2}$  and an angle of attack  $\alpha_a = \alpha - \theta_{geom}$  where angle  $\alpha$  is derived from the relation  $\alpha = \arctan2(v_y, v_x)$ , with:

- $v_y = r\omega_p$
- $v_x = v_\infty$

The local pressure is computed using the following relation:  $p_l = \frac{1}{2}\rho v_a^2 C_p(r, \alpha_a(r), v_a(r))$

#### 3.2.1. Bidimensional fluid solver

The fluid is modeled as a perfect fluid, potential solutions are considered and the singularity superposition method is applied (as in Xfoil Drela, 1989 or Katz and Plotkin, 2001). Two elementary solutions are used: the vortex of intensity  $\gamma$  and of velocity potential  $\phi^v$  and masses of intensity  $\sigma$  and of velocity potential  $\phi^m$ . The vortex singularities models in a straightforward fashion lift phenomenon. The velocity potential of the flow around a section  $\mathcal{P}$  is:

$$\Phi(x, y) = v_a(\cos(\alpha_a)x + \sin(\alpha_a)y) + \int_{\mathcal{P}} \gamma(s)\phi^v(x, y, s)ds + \int_{\mathcal{P}} \sigma(s)\phi^m(x, y, s)ds \quad (35)$$

where vortex density  $\gamma$  and masses density  $\sigma$  are the unknown to be computed.

The Annexe A shows how Eq. (35) is discretized and how the vortex and mass density are determined. The velocity field can then be computed and Bernoulli law gives the pressure coefficient at each point  $(x, y)$ :  $C_p(x, y) = 1 - (v(x, y)/v_\infty)^2$ . As the fluid is considered inviscid, the drag coefficient  $C_d = \int_{\mathcal{P}} p \langle \mathbf{n}, e_x \rangle = 0$ . The Kutta–Joukowski theorem gives a very convenient way of computing the local lift coefficient:  $C_l = \frac{2\Gamma}{v_\infty}$  where  $\Gamma = \int_{\mathcal{P}} \gamma(s)ds$

#### 3.2.2. Numerical solving process

The blade element method therefore simplifies the fluid problem resolution by splitting the 3D problem into multiple 2D problems. This method can be coupled to a finite element method solver  $S$ , following these two steps:

1. First of all, the section must be extracted from the 3D mesh of the blade (eventually deformed with a displacement field  $\mathbf{u}_1$ ). The sections are extracted by computing the intersections of the surface element of the mesh with a cylinder centered on the hub and of radius  $r$  (see Fig. 5). This operation is not numerically costly and does not constraint the 3D mesh of the blade.
2. On each section computed, the flow  $(v_a, \alpha)$  is computed, the matrix equation (62) is constructed and solved. The pressure field evaluated on each section is projected onto the whole mesh.

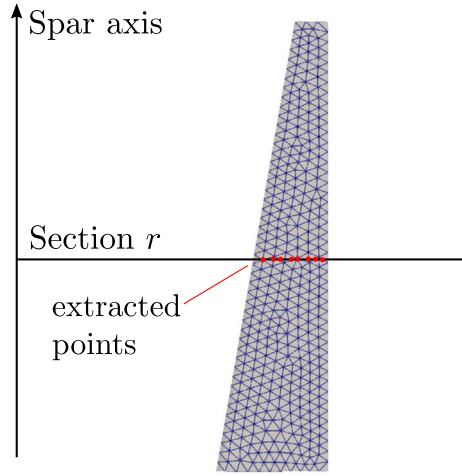


Fig. 5. Extraction of the blade sections.

These steps constitute the fluid solver  $\mathcal{F}$ :

$$p_1 = \mathcal{F}(\mathbf{u}_1) \quad (36)$$

### 3.3. Structure solver, finite element method

The nonlinear structure problem is solved using the finite element method, this resolution is based on the weak form of the equation which reads on configuration  $C_1$ :

Find  $\mathbf{u}_1$ , for all  $\mathbf{v}$

$$\int_{\Omega^s} \rho \langle (\omega_p \mathbf{R})^2 (\mathbf{x}_0 + \mathbf{u}_1), \mathbf{v} \rangle + \int_{\Omega^s} \boldsymbol{\sigma}_1(\mathbf{u}_1) : \mathbf{v} = \int_{\partial\Omega^s} \langle p_1 \mathbf{n}_1(\mathbf{u}_1), \mathbf{v} \rangle \quad (37)$$

Three operators are considered:

1. The gyroscopic operator

$$W_g(\mathbf{u}_1, \mathbf{v}) = \int_{\Omega^s} \rho \langle (\omega_p \mathbf{R})^2 (\mathbf{x}_0 + \mathbf{u}_1), \mathbf{v} \rangle \quad (38)$$

2. The internal stress power operator

$$W_{int}(\mathbf{u}_1, \mathbf{v}) = \int_{\Omega^s} \boldsymbol{\sigma}_1(\mathbf{u}_1) : \mathbf{v} \quad (39)$$

3. The external stress power operator

$$W_{ext}(\mathbf{u}_1, \mathbf{v}) = \int_{\partial\Omega^s} \langle p_1 \mathbf{n}_1(\mathbf{u}_1), \mathbf{v} \rangle \quad (40)$$

The internal and external stress power operators are nonlinear with respect to the displacement  $\mathbf{u}_1$  and the pressure field is modeled by a *follower load* meaning that  $p = p \circ \phi_{20}$ . The Appendix B shows how Eq. (37) is discretized in weak form using finite method. At a given hydrodynamic pressure load  $p$ , the nonlinear static problem reads:

Find  $\mathbf{U}_1$ , such that:

$$\langle \mathbf{F}^{int}(\mathbf{U}_1), \mathbf{V} \rangle + \langle \mathbf{K}_c \mathbf{U}_1, \mathbf{V} \rangle = \langle \mathbf{F}^{ext}(\mathbf{U}_1), \mathbf{V} \rangle - \langle \mathbf{F}^g, \mathbf{V} \rangle \text{ for all } \mathbf{V} \quad (41)$$

As Eq. (41) must be true for all  $\mathbf{V}$ , it can be expressed as a nonlinear vector equation:

$$\mathbf{F}^{int}(\mathbf{U}_1) + \mathbf{K}_c \mathbf{U}_1 = \mathbf{F}^{ext}(\mathbf{U}_1) - \mathbf{F}^g \quad (42)$$

This equation is then solved by a Newton–Raphson algorithm, these operations compose the structure operator  $S$ :

$$\mathbf{u}_1 = S(p_1) \quad (43)$$

## 4. Solver for the vibroacoustic problem

### 4.1. Monolithic formulation

The vibroacoustic phenomenon equations (Eq. (33)) can be solved with finite element method in a monolithic  $u - \psi$  formulation (Everstine, 1981). To take into account an infinite fluid domain, the BGT (Bayliss et al., 1982) conditions are used on the boundary  $\Gamma_\infty$  of the spherical fluid domain of radius  $R$ :

$$\langle \nabla \psi_2, \mathbf{n}_1 \rangle + \left( \frac{i\omega}{c} + \frac{1}{R} \right) \psi_2 = 0 \quad (44)$$

The monolithic  $u - \psi$  finite element method is used. As the displacement  $\mathbf{u}_2$  is small, the actual configuration  $C_2$  and the intermediate configuration  $C_1$  are very close to one another and the weak formulation of the problem is solved on configuration  $C_1$ :

- Find  $\mathbf{u}_2$ , such as:

$$-\omega^2 \int_{\Omega^s} \rho_s \langle \mathbf{u}_2, \mathbf{v} \rangle + \int_{\Omega^s} \boldsymbol{\sigma}_2 : \nabla \mathbf{v} + i\omega \int_{\partial\Omega^s} \rho \psi_2 \langle \mathbf{v}, \mathbf{n}_1 \rangle = \int_{\Gamma^{\text{excit}}} p^{\text{excit}} \langle \mathbf{v}, \mathbf{n}_1 \rangle \text{ for all } \mathbf{v} \quad (45)$$

- Find  $\psi_2$ , such as:

$$-\omega^2 \int_{\Omega^f} \frac{\rho}{c^2} \psi_2 \phi + \int_{\Omega^f} \rho \nabla \psi_2 \nabla \phi + \left( i\omega + \frac{c}{R} \right) \int_{\Gamma_\infty} \frac{\rho}{c} \psi_2 \phi - i\omega \int_{\partial\Omega^s} \rho \langle \mathbf{u}_2, \mathbf{n}_1 \rangle \phi = 0 \text{ for all } \phi \quad (46)$$

### 4.2. Structural equations

The structural equation (Eq. (45)) has three operators written on configuration  $C_1$  that need to be discretized:

- Mass bilinear form:  $m(\mathbf{u}_2, \mathbf{v}) = \int_{\Omega^s} \rho_s \langle \mathbf{u}_2, \mathbf{v} \rangle$
- Stress power bilinear form:  $W(\mathbf{u}_2, \mathbf{v}) = \int_{\Omega^s} \boldsymbol{\sigma}_2(\mathbf{u}_2) : \nabla_1 \mathbf{v}$
- Fluid–structure coupling bilinear form:  $c(\psi_2, \mathbf{v}) = \int_{\partial\Omega^s} \rho \psi_2 \langle \mathbf{v}, \mathbf{n} \rangle$
- The imposed pressure linear form:  $f(\mathbf{v}) = \int_{\Gamma^{\text{excit}}} p^{\text{excit}} \langle \mathbf{v}, \mathbf{n} \rangle$

The mass, coupling and imposed pressure operator can be discretized on configuration  $C_1$  as:

$$m(\mathbf{u}_2, \mathbf{v}) \Rightarrow \langle \mathbf{M} \mathbf{U}_2, \mathbf{V} \rangle$$

$$c(\psi_2, \mathbf{v}) \Rightarrow \langle \mathbf{C} \boldsymbol{\Psi}_2, \mathbf{V} \rangle$$

and

$$f(\mathbf{v}) \Rightarrow \langle \mathbf{P}^{\text{excit}}, \mathbf{V} \rangle$$

Matrices  $\mathbf{M}$  and  $\mathbf{C}$  are called mass matrix and coupling matrix and  $\mathbf{P}^{\text{excit}}$  the force vector.

The stress power operator must be considered here with extra care. The stress tensor  $\boldsymbol{\sigma}_2$  has two contribution: a geometrical one and material one. Therefore the operator is split into two contributions:

$$W(\mathbf{u}_2, \mathbf{v}) = \underbrace{\int_{\Omega^s} \frac{1}{J_0} \mathbf{F}_0 d\mathbf{S}_{u_1}(\mathbf{u}_2) \mathbf{F}_0^T : \boldsymbol{\epsilon}(\mathbf{v})}_{W^{\text{mat}}} + \underbrace{\int_{\Omega^s} (\nabla_1 \mathbf{u}_2) \boldsymbol{\sigma}_1 : \nabla_1(\mathbf{v})}_{W^{\text{geom}}} \quad (47)$$

The operator  $W^{\text{mat}}$  can be rewritten on configuration  $C_0$  and reads:

$$W^{\text{mat}}(\mathbf{u}_2, \mathbf{v}) = \int_{\Omega^s} d\mathbf{S}_{u_1}(\mathbf{u}_2) : \mathbf{E}^v(\mathbf{u}_1, \mathbf{v}) \quad (48)$$

where,  $\mathbf{E}^v(\mathbf{u}_1, \mathbf{v}) = 1/2(\mathbf{F}_0^T \nabla_1 \mathbf{v} + (\nabla_1 \mathbf{v})^T \mathbf{F}_0)$  (see Appendix B). Using the following relations:

- $\nabla_1 \mathbf{u}_2 = (\nabla_0 \mathbf{u}_2) \mathbf{F}_0^{-1}$
- $\nabla_1 \mathbf{v} = (\nabla_0 \mathbf{v}) \mathbf{F}_0^{-1}$
- $\mathbf{A} \mathbf{C}^T : \mathbf{B} = \mathbf{A} : \mathbf{B} \mathbf{C}$

the geometrical contribution can be rewritten as  $W^{\text{geom}}(\mathbf{u}_2, \mathbf{v}) = \int_{\Omega^s} (\nabla_0 \mathbf{u}_2) \mathbf{S}(\mathbf{u}_1) : \mathbf{F}^v$ . The symmetry of tensor  $\mathbf{S}$  yields:

$$\begin{aligned} W^{\text{geom}}(\mathbf{u}_2, \mathbf{v}) &= \int_{\Omega^s} \mathbf{S}(\mathbf{u}_1) : \frac{1}{2} ((\nabla_0 \mathbf{u}_2)^T \nabla_1 \mathbf{v} + (\nabla_1 \mathbf{v})^T \nabla_0 \mathbf{u}_2) \\ &= \int_{\Omega^s} \mathbf{S}(\mathbf{u}_1) : d\mathbf{E}_{u_1}^v(\mathbf{u}_2, \mathbf{v}) \end{aligned}$$

Therefore, the stress power operator has the following expression on configuration  $C_0$ :

$$W(\mathbf{u}_2, \mathbf{v}) = \int_{\Omega^s} dS_{\mathbf{u}_1}(\mathbf{u}_2) : \mathbf{E}^v(\mathbf{u}_1, \mathbf{v}) + \mathbf{S}(\mathbf{u}_1) : d\mathbf{E}_{\mathbf{u}_1}^v(\mathbf{u}_2, \mathbf{v}) \quad (49)$$

This is the same expression as in Eq. (67), the stress power operator of the vibroacoustic phenomenon  $W(\mathbf{u}_2, \mathbf{v})$  is the differential of the internal stress power operator  $dW_{\mathbf{u}_1}^{\text{int}}(\mathbf{u}_2, \mathbf{v})$ . In most finite element method software, a features that computes this operator already exists, no specific costly numerical development is therefore needed, note that this operator must be built on the initial configuration  $C_0$  (in other word on the undeformed mesh). The discretized structural equation in weak form therefore reads:

Find  $\mathbf{U}_2$ , such that:

$$-\omega^2 \langle \mathbf{M}\mathbf{U}_2, \mathbf{V} \rangle + i\omega \langle \mathbf{C}\Psi_2, \mathbf{V} \rangle + \langle \mathbf{K}^{\text{int}}(\mathbf{U}_1)\mathbf{U}_2, \mathbf{V} \rangle = \langle \mathbf{P}^{\text{excit}}, \mathbf{V} \rangle \text{ for all } \mathbf{V} \quad (50)$$

The corresponding strong formulation takes the form of the following matrix system:

$$-\omega^2 \mathbf{M}\mathbf{U}_2 + i\omega \mathbf{C}\Psi_2 + \mathbf{K}^{\text{int}}(\mathbf{U}_1)\mathbf{U}_2 = \mathbf{P}^{\text{excit}} \quad (51)$$

### 4.3. Fluid equations

The fluid equation in weak form has four bilinear operators that need to be discretized, on configuration  $C_1$ . They take the form:

- fluid mass bilinear form  $g(\psi_2, \phi) = \int_{\Omega^f} \frac{\rho}{c^2} \psi_2 \phi$  which is discretized into:

$$g(\psi_2, \phi) \Rightarrow \langle \mathbf{G}\Psi_2, \Phi \rangle$$

- fluid rigidity bilinear form  $h(\psi_2, \phi) = \int_{\Omega^f} \rho \nabla(\psi_2) \nabla(\phi)$  which is discretized into:

$$h(\psi_2, \phi) \Rightarrow \langle \mathbf{H}\Psi_2, \Phi \rangle$$

- impedance bilinear form  $q(\psi_2, \phi) = \int_{\Gamma_\infty} \frac{\rho}{c} \psi_2 \phi$  which is discretized into:

$$q(\psi_2, \phi) \Rightarrow \langle \mathbf{Q}\Psi_2, \Phi \rangle$$

- fluid–structure coupling bilinear operator  $c(\phi, \mathbf{u}_2) = \int_{\partial\Omega^s} \rho \langle \mathbf{u}_2, \mathbf{n}_1 \rangle \phi$  which is discretized into:

$$c(\phi, \mathbf{u}_2) \Rightarrow \langle \mathbf{C}^T \mathbf{U}_2, \Phi \rangle$$

The discretized fluid problem then reads:

Find  $\Psi_2$ , such as:

$$-\omega^2 \langle \mathbf{G}\Psi_2, \Phi \rangle + i\omega (-\langle \mathbf{C}^T \mathbf{U}_2, \Phi \rangle + \langle \mathbf{Q}\Psi_2, \Phi \rangle) + \langle \mathbf{H}\Psi_2, \Phi \rangle + \frac{c}{R} \langle \mathbf{Q}\Psi_2, \Phi \rangle = 0 \text{ for all } \Phi \quad (52)$$

The corresponding strong formulation yields the following matrix system:

$$-\omega^2 \mathbf{G}\Psi_2 + i\omega (-\mathbf{C}^T \mathbf{U}_2 + \mathbf{Q}\Psi_2) + \mathbf{H}\Psi_2 + \frac{c}{R} \mathbf{Q}\Psi_2 = 0 \quad (53)$$

### 4.4. Numerical solving method

The combination of matrix system ((51), (53)) gives the symmetric monolithic formulation of the vibro-acoustic phenomenon:

$$\left[ -\omega^2 \begin{pmatrix} \mathbf{M} & \mathbf{0} \\ \mathbf{0} & -\mathbf{G} \end{pmatrix} + i\omega \begin{pmatrix} \mathbf{0} & \mathbf{C} \\ \mathbf{C}^T & -\mathbf{Q} \end{pmatrix} + \begin{pmatrix} \mathbf{K}^{\text{tan}}(\mathbf{U}_1) & \mathbf{0} \\ \mathbf{0} & -\mathbf{H} - \frac{c}{R} \mathbf{Q} \end{pmatrix} \right] \begin{pmatrix} \mathbf{U}_2 \\ \Psi_2 \end{pmatrix} = \begin{pmatrix} \mathbf{P}^{\text{excit}} \\ \mathbf{0} \end{pmatrix} \quad (54)$$

## 5. Numerical application of the methodology

This methodology is implemented in an in-house python (Van Rossum and Drake, 2009) library. The procedures of code\_aster (EDF, 1989) are used for the assembly of the structural and vibroacoustic matrix systems which are solved using MUMPS (Amestoy et al., 2002). The blade element method was implemented in python using NumPy (Harris et al., 2020) for all vectorizable operation and Cython (Behnel et al., 2011) when vectorization was not possible. All computations are parallelized using OpenMP protocols (Chandra et al., 2001).

This formulation is applied to a simplified one meter long blade with NACA0006 sections. The chord of the sections varies in a linear way: the root is 250 mm long and the blade tip is 75 mm long. The geometry of the blade is fairly simple but remains representative of a real propeller blade. Fig. 6(a) shows the CAD of the blade.

The blade suffers the following static flow:

- ship's velocity:  $v_\infty = 8 \text{ m s}^{-1}$
- rotation velocity:  $\omega_p = 0.8 \text{ rad s}^{-1}$

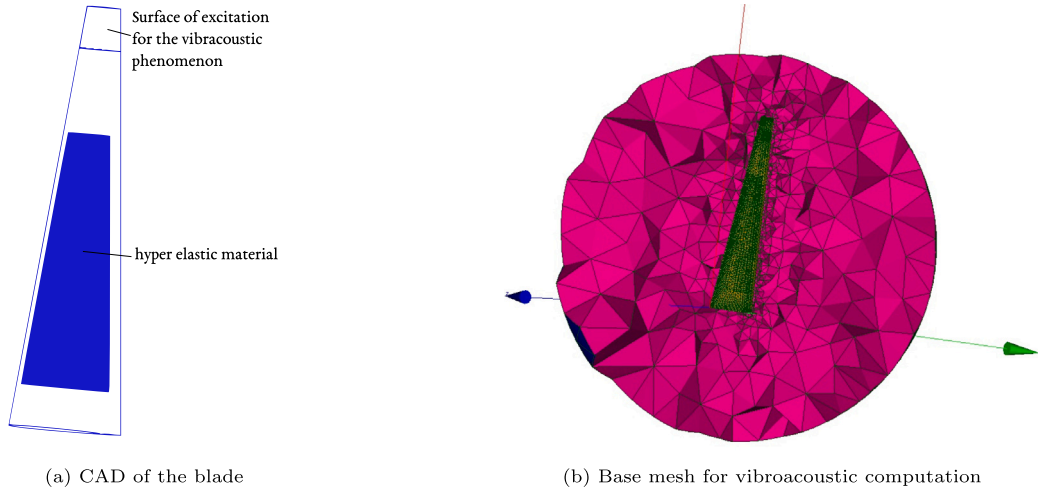


Fig. 6. CAD of the propeller and base mesh used in every computation.

**Table 1**  
Material and fluid properties of the test case.

Water		Aluminum		Hyperelastic material	
$\rho_f$	1000 kg m <sup>-3</sup>	$E$	65 GPa	$C_{10}$	0.238 MPa
$c_0$	1500 m s <sup>-1</sup>	$\nu$	0.36	$C_{01}$	0.532 MPa
		$\rho$	2500 kg m <sup>-3</sup>	$K$	2.1 GPa
		Constitutive law	Saint-Venant Kirchhoff	$\rho$	1400 kg m <sup>-3</sup>
				Constitutive law	Mooney–Rivlin

The hub is 0.2 m long, therefore the angle of attack at the tip blade is 8°, the tip section is therefore under the stall limit and the flow remains unseparated. The harmonic excitation is simplified in this numerical application, a uniform pressure is applied on one side of the blade between 0.9 m and 1 m. The fluid is water, the blade is made of aluminum and a film of visco-elastic material is inserted inside the blade, its shape and position within the blade is shown in Fig. 6(a). Table 1 gives the materials and fluid properties used.

The simplified geometry of the structure allows to test the proposed numerical approach, while being representative of the end application. The visco-elastic material has frequency-dependent moduli in the Fourier space, However, for the sake of simplicity these variation will not be taken into account: in this work the focus is put on the effect of the pre-stress and pre-strain on the vibrational characteristics. The damping characteristics of the hyper-visco-elastic layer is the object of a companion paper. The propulsion problem is solved twice using two different algorithms. First a *weak coupling* computation is done, the fluid solver and structural solver are chained, and the retroaction of the blade's deformation on the flow is neglected. Then an iterative *strong coupling* computation is carried out, the simple iterative coupling algorithm is applied until convergence. The vibroacoustic problem is solved on three different configurations:

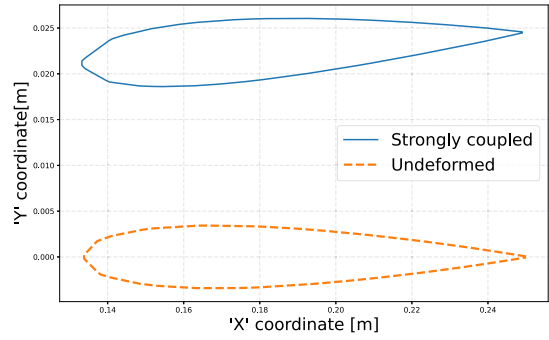
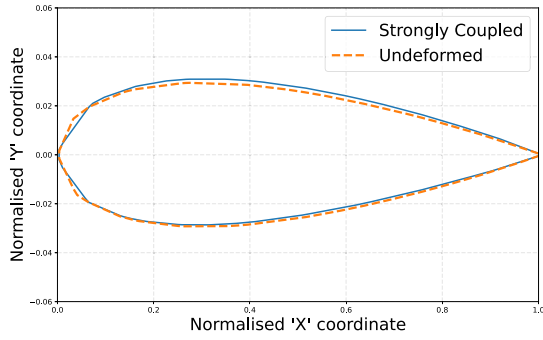
- First on the reference configuration, a classical  $u - \Psi$  system is solved on the *undeformed mesh*.
- Then on the configuration  $C_1$  without pre-stress and without pre-strain, a classical  $u - \Psi$  system is solved on the *deformed mesh*. The configuration  $C_1$  is computed by the solving of system (34)
- At last, on configuration  $C_1$  taking into account the pre-stress and pre-strain generated by the propulsion phenomenon computation. The system (34) is first solved to compute the deformed mesh and the pre-stress tensor. Then the modified  $u - \Psi$  system (54) is solved.

### 5.1. Propulsion phenomenon

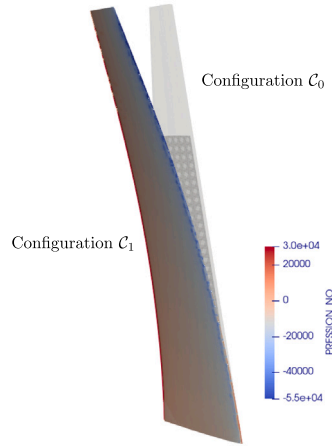
For both the weakly coupled and strongly coupled computations, 50 hydrodynamic sections are extracted from the mesh. In the strongly coupled computation, this extraction must be carried out at each iteration, which remained cheap compared to the individual fluid (62) and structural (42) problem resolution. The strongly coupled computation converges to a relative error of  $5 \cdot 10^{-4}$  on the displacement field in 9 iterations. At each iteration, the structure solver initializes the Newton–Raphson algorithm with the previous solution, this allows to decrease significantly the total computation time.

To measure the true deformation of the section, the normalized section is analyzed. It corresponds to a section normalized by its chord and represented with its leading edge put at the origin and its trailing edge at point (1, 0). The Fig. 7(a) shows a comparison between normalized blade tip sections extracted from the initial configuration and configuration  $C_1$ . The pure deformation of the





(a) True deformation on the normalized section at wing tip for the strongly coupled computation, comparison with the initial configuration  
 (b) Full deformation on the normalized section at wing tip for the strongly coupled computation, comparison with the initial configuration



(c) Deformation of the whole blade and pressure field at the wetted surface

Fig. 7. Effect of the fluid/structure interaction on the structural deformation.

section remains small, it shows However, a positive camber increase. Fig. 7(b) displays the section as extracted from the mesh, the full deformation of the section is mainly a translation and a blade angle (about  $-1.3^\circ$ ) is added to the section. This change in blade angle is significant and a modification of the local load is expected. Fig. 8 shows the evolution of the coefficient of lift  $C_L$  along the wingspan. As expected, the load of the strongly and weakly coupled computations are quite different. In weakly coupled computation the geometry of the blade is not deformed, the angle of attack  $\alpha$  at each section  $z$  is  $\arctan(z\omega/V_\infty) \sim z\omega/V_\infty$  and in the attached flow regime, the NACA 0006 lift coefficient can be approached by  $C_L = 2\pi\alpha$ , therefore the load is almost linear with  $Z$  coordinate. The load of the strongly coupled computation is not linear with  $z$ , the positive camber increase creates a lift generation increase at the root of the blade. Closer to the tip of the blade, this effect is mitigated by the negative blade angle and the lift generation is much lower than in the chained computation. Here the deformation of the blade has a overall negative effect on the performances.

From the structural point of view, the displacement of the wingtip is about 130 mm which is significant and the viscoelastic layer suffers a 3% strain. The global movement is a flexion of the blade, the viscoelastic film However, suffers a shear in the  $xz$  plane. Fig. 7(c) shows a comparison of the deformed and initial structure.

### 5.2. Vibroacoustic phenomenon

The vibroacoustic phenomenon is studied on the frequency range [100, 200] Hz with a 0.05 Hz frequency step. A global hysteric damping of 0.01% added. Three computations were carried on different configuration and different modeling hypothesis:

- [I] Configuration  $C_0$
- [II] Configuration  $C_1$ , no pre-stress or pre-strain (small perturbation hypothesis)
- [III] Configuration  $C_1$ , with pre-stress and pre-strain

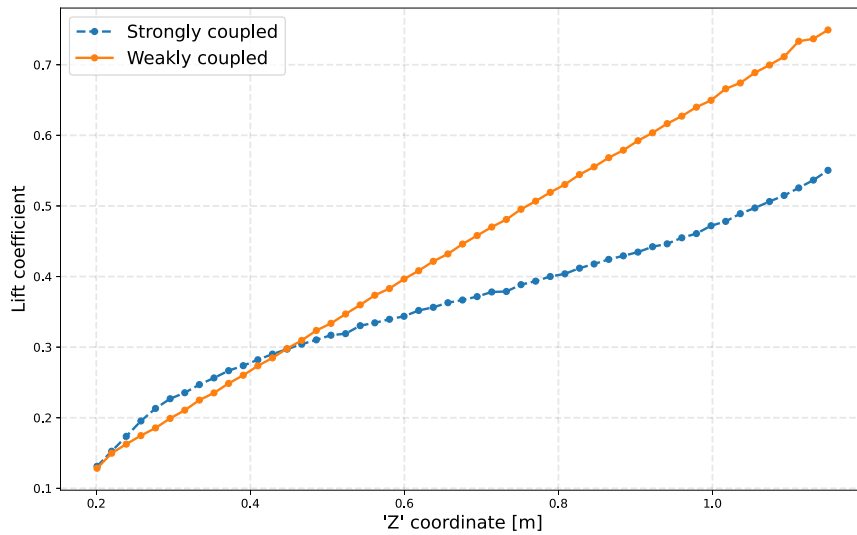


Fig. 8. Adimensional local lift coefficient along the blade's spar for the strongly and weakly coupled computation.

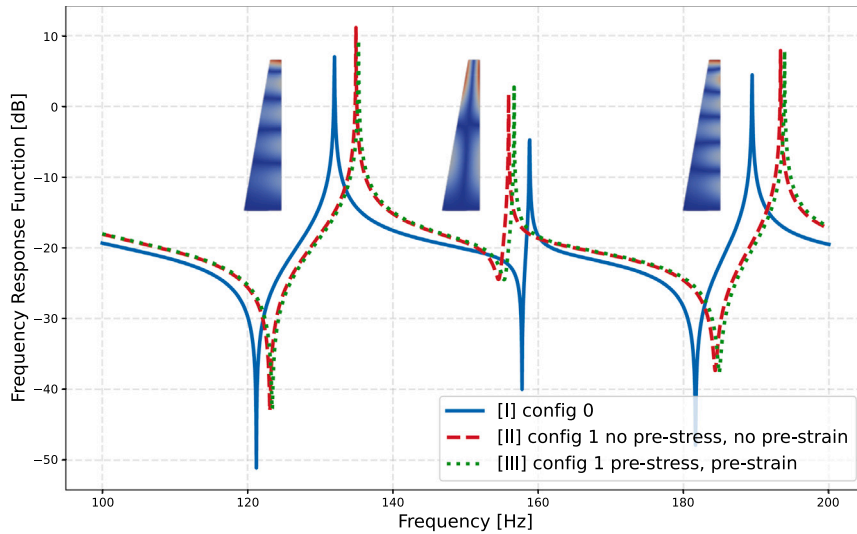


Fig. 9. Frequency response function on the reference configuration, the deformed configuration without pre-stress and without pre-stress and on the deformed configuration with both pre-stress and pre-strain. The modal deformation on the reference configuration is displayed for each peak.

We use a common base mesh for all the configurations, it is computed on the initial configuration surrounded by a sphere of fluid. The mesh for the deformed configuration is computed using the pseudo material method (Boncoraglio et al., 2021). Fig. 6(b) shows the base mesh used in all computations, it is made of  $\sim 2.3 \cdot 10^5$  nodes and  $\sim 1.7 \cdot 10^5$  quadratic tetrahedral elements with 10 points. The Fig. 10 shows the sound power spectrum of the three computations. The displacement field of each modes is displayed. The first and third modes are bending modes and the second mode is a torsion mode. The computation [I] and [III] shows significant differences in the sound power spectrum. On configuration  $C_1$ , the torsion mode is shifted towards lower frequencies and the bending modes are shifted towards higher frequency. The amplitudes are also globally higher on this configuration. The computations [II] and [III] gives similar results in this case. Therefore the change of geometry is the main effect at play here, the pre-strain and pre-stress shifts the power spectrum towards slightly higher frequencies. The same conclusions can be drawn from the frequency response function displayed in Fig. 9.

### 5.3. Discussion

The most critical steps of the methodology were compared to experimental studies in order to evaluate the different hypothesis. Composite blades were built and tested in Ecole Centrale Nantes tow tank, the deformation (using fiber Bragg grating sensors)

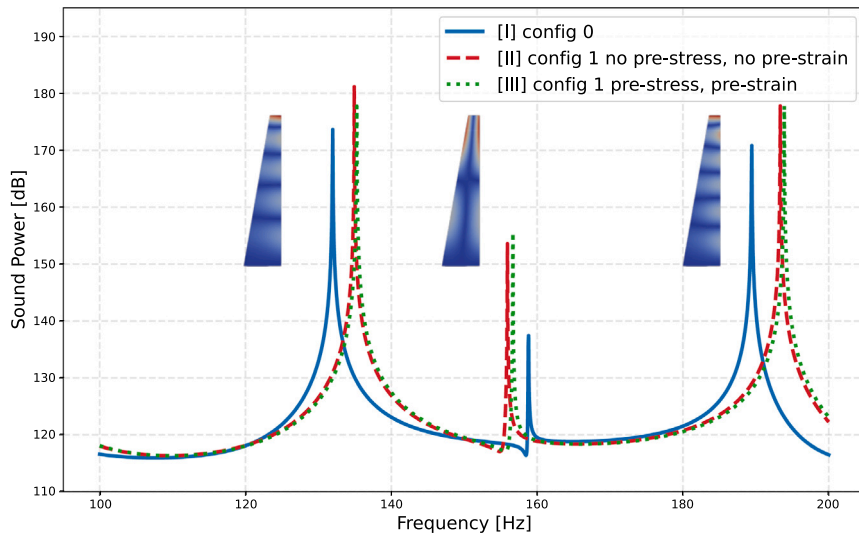


Fig. 10. Sound power computed on the reference configuration, the deformed configuration without pre-strain and without pre-stress and on the deformed configuration with both pre-stress and pre-strain. The modal deformation on the reference configuration is displayed for each peak.

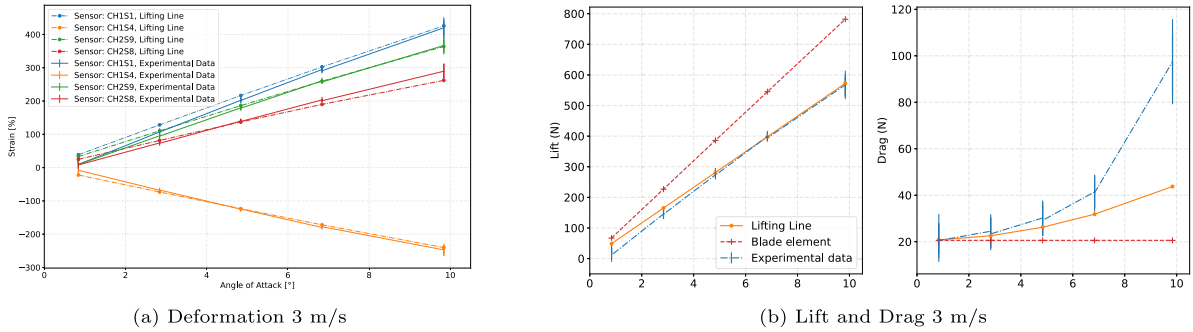


Fig. 11. Comparison between the experimental results and the numerical computations on the monolithic blade.

and hydrodynamic forces (using a hydrodynamic balance) are compared. A first conference paper was submitted to CSMA 2024 (Rakotomalala et al., 2024), a correlation between experimental and numerical data is proposed regarding the so-called propulsion phenomenon. Figs. 11(a) and 11(b) are extracted from this conference paper.

They show that if the simplified element method yields lift and drag very different from the measured data, a more sophisticated lifting line blade element method can match the measurement on lift and drag data. Using this improved fluid model, the strongly coupled algorithm is also able to compute deformations along the blade that matches the measured data.

Another experiment was carried out to evaluate the simplified formulation of the stress tensor for vibration under pre-stress and pre-strain. Composite plates were built and tested on an in-house experimental setup that allows to measure the FRF of these plates with a given torsional pre-strain. This is the subject of a dedicated article currently being written.

This paper aims at presenting a simplified model that can be used to compute a specific noise contribution of a propeller in a specific industrial problem. The fluid model was simplified to large extent to illustrate the methodology, a more sophisticated fluid model could be used. However, for the specific propeller geometry and operating conditions considered, the hypothesis of a lifting line model is reasonable and representative of the physics at stake.

### 6. Conclusions and perspectives

This approach aims at representing both the large deformation of the structure and its small vibrations in the fluid in a simplified manner. Therefore both the steady nonlinear interaction between an incompressible fluid and a structure and the noise radiated by small vibrations of the pre-stressed structure can be computed as a whole. Effects of the change in geometry and material stress on the vibrations can then be evaluated. Within the hypothesis of this study, the approach was mathematically proven to be valid. The propeller suffers two main phenomena: the *propulsion phenomenon* which takes into account the nonlinear strain due to the lift generation along the section of the propeller and the *vibroacoustic phenomenon* which describes the linear interaction between

the vibrating structure and the acoustic fluid on the pre-strained and pre-stressed structure. The two phenomena are chained: the propulsion phenomenon resolution gives the pre-strain and pre-stress as input for the vibroacoustic phenomenon which does not have a retro-action on the nonlinear problem. This approach was implemented in a python library and illustrated on a simplified blade geometry. The noise emission of a deformed flexible propeller blade can be significantly different from its emission at rest. The geometrical deformation seems to be of first order whereas the pre-stress seems to be of second order in the case of metallic propeller's blade.

In this approach, the vibrations of the structure are caused by given oscillating pressures applied a surface of the blade chosen in order to stimulate the different modes of the structure. This pressure field is not physical but give ideas on the acoustical signature of the blades in a straightforward manner. In reality, the excitation comes from the pressure fluctuations of the turbulent boundary layer, two approaches could be considered. First, the fluctuating pressure fields could be computed using fully resolved LES computation, the pressure field would therefore be deterministic. It would However, require to carry out a very expensive computation for each change of steady state of the blade. This problem could be tackled by the construction of a metamodel of the fluctuating pressure field using a limited number of LES computations in an offline phase. Another approach could be to carry out stochastic computations using turbulent pressure spectrum models.

This model needs as input a constitutive law for the damping material that takes into account the material nonlinear static properties and the linear vibrations characteristics around the static pre-stressed and pre-strained configuration. Such an hyper-visco-elastic constitutive law must therefore be determined, which is the topic of a companion paper.

The computation time of the propulsion phenomenon are reasonable because of the simplified fluid model used, However, the vibroacoustic phenomenon computation complexity can be off-putting as the number of degrees of freedom can be important on an industrial geometry and the frequency range considered can be huge, reduction model methods like proper orthogonal decomposition, reduce basis (Maday and Stamm, 2013) and neural networks might be used to lower the computational costs.

### CRedit authorship contribution statement

**Quentin Rakotomalala:** Writing – review & editing, Writing – original draft, Validation, Software, Formal analysis, Conceptualization. **Lucie Rouleau:** Writing – review & editing, Writing – original draft, Validation. **Cédric Leblond:** Writing – review & editing, Writing – original draft, Validation, Supervision. **Mickaël Abbas:** Writing – original draft, Software. **Jean-François Deü:** Writing – review & editing, Validation.

### Declaration of competing interest

The authors declare the following financial interests/personal relationships which may be considered as potential competing interests: Quentin Rakotomalala reports financial support was provided by Naval Group.

### Data availability

No data was used for the research described in the article.

### Acknowledgments

We thank Astrid Filiot and Guillaume Dolo for the useful discussion regarding mechanics and software development. This study is financed by Naval Group and the ANRT through a doctoral study grant in collaboration with le Cnam.

### Appendix A. Bidimensional fluid solver

The 2D flow around the blade section derives from a potential:

$$\Phi(x, y) = v_a(\cos(\alpha_a)x + \sin(\alpha_a)y) + \int_{\mathcal{P}} \gamma(s)\phi^v(x, y, s)ds + \int_{\mathcal{P}} \sigma(s)\phi^m(x, y, s)ds \quad (55)$$

where  $\gamma$  and  $\sigma$  are vortex and mass distribution that needs to be determined. The lifting section  $\mathcal{P}$  is discretized in  $N$  panels, for  $0 \leq i \leq N-1$ , panels  $\mathcal{P}_i$  is the segment  $(x_i, x_{i+1})$ , panel  $\mathcal{P}_{N-1}$  represents the trailing panel  $(x_{N-1}, x_0)$ . In this paper, only thick trailing edge is considered therefore  $x_{N-1} \neq x_0$ . The density  $\gamma$  is approached by a linear function on each panel and function  $\sigma$  is taken as constant with value  $\sigma^{te}$  on the trailing edge panel. The sum  $\int_{\mathcal{P}} \sigma(s)ds$  must be null as the section neither create nor consume fluid, therefore we take  $\sigma|_{\mathcal{P}_i} = -\sigma^{te} \frac{l_{N-1}}{l_i}$  where  $l_i$  is the length of panel  $\mathcal{P}_i$

**Remark.** The index  $i + 1$  will be taken as its congruence modulo  $N$ . This allows to take into account the trailing edge panel in a straightforward manner (see Fig. 12).

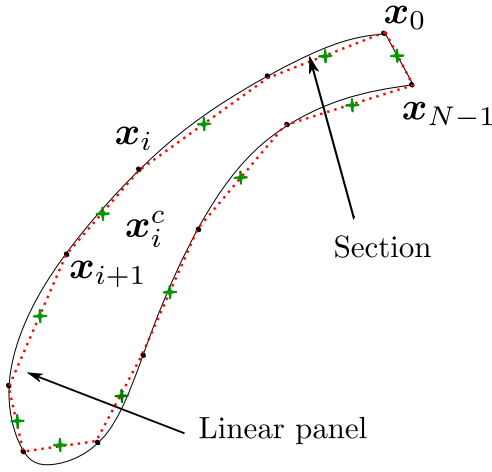


Fig. 12. Section discretized in panels.

The potential is therefore split on each panel  $\mathcal{P}_i$ :

$$\begin{aligned} \Phi(x, y) &= v_a(\cos(\alpha_a)x + \sin(\alpha_a)y) + \sum_{i=0}^{N-1} \int_{\mathcal{P}_i} \gamma(s)\phi^v(x, y, s)ds + \int_{\mathcal{P}_i} \sigma(s)\phi^m(x, y, s)ds \\ &= v_a(\cos(\alpha_a)x + \sin(\alpha_a)y) + \sum_{i=0}^{N-1} \Phi_i^v(x, y) + \sum_{i=0}^{N-1} \Phi_i^m(x, y) \end{aligned}$$

where  $\Phi_i^v$  (respectively  $\Phi_i^m$ ) is the panel  $\mathcal{P}_i$  contribution to the vortex (respectively to the mass). Each panel  $\mathcal{P}_i$  is parameterized using its curvilinear abscissa  $s$  normalized in the interval  $[-1, 1]$ , and each point of a panel is approached by  $\mathbf{x}(s) = \frac{x_{i+1}-x_i}{2}s + \frac{x_{i+1}+x_i}{2}$

On each panel  $\mathcal{P}_i$  the density of vortex is linear with respect to  $s$ :  $\gamma|_{\mathcal{P}_i}(s) = \frac{\gamma_{i+1}-\gamma_i}{2}s + \frac{\gamma_{i+1}+\gamma_i}{2}$ , the vortex contribution  $\Phi_i^v$  therefore reads:

$$\Phi_i^v(x, y) = \frac{l_i}{4\pi} \int_{-1}^1 \gamma(s)\theta(\mathbf{x} - \mathbf{x}_s)ds \tag{56}$$

where  $\theta(\mathbf{r})$  is the angle between  $\mathbf{r}$  and a given axis of reference  $\mathbf{e}_x$ . Fig. 13 shows that angle  $\theta$  depends on the panel angle  $\theta_i$  and the local coordinates  $(\bar{x}, \bar{y})$  in the reference axis of the panel:

$$\theta(\mathbf{x} - \mathbf{x}_s) = \theta_i + \arctan 2(\bar{y}, \bar{x} - 0.5l_i s) \tag{57}$$

The contribution of  $\Phi_i^v$  to the panel  $\mathcal{P}_i$  therefore reads:

$$\Phi_i^v(x, y) = \frac{\gamma_{i+1} + \gamma_i}{2} \phi_i^{v+}(x, y) + \frac{\gamma_{i+1} - \gamma_i}{2} \phi_i^{v-}(x, y) \tag{58}$$

where

- $\phi_i^{v+}(x, y) = \frac{l_i}{4\pi} \int_{-1}^1 \theta_i + \arctan 2(\bar{y}, \bar{x} - 0.5l_i s)ds$
- $\phi_i^{v-}(x, y) = \frac{l_i}{4\pi} \int_{-1}^1 \arctan 2(\bar{y}, \bar{x} - 0.5l_i s)ds$

On each panel  $\mathcal{P}_i$ , the mass density is constant with value  $\sigma_i$ , the contribution  $\Phi_i^m$  therefore reads:

$$\Phi_i^m(x, y) = \sigma_i \phi_i^m(x, y) \tag{59}$$

where:  $\phi_i^m(x, y) = \frac{l_i}{8\pi} \int_{-1}^1 \ln(\bar{y}^2 + (\bar{x} - 0.5l_i s)^2)ds$

The velocity field is the spatial gradient of the potential:

$$\begin{aligned} \mathbf{v}(x, y) &= v_\infty (\cos(\alpha)\mathbf{e}_x + \sin(\alpha)\mathbf{e}_y) + \sum_{i=0}^{N-1} \frac{\gamma_{i+1} + \gamma_i}{2} \mathbf{v}_i^+(x, y) + \sum_{i=0}^{N-1} \frac{\gamma_{i+1} - \gamma_i}{2} \mathbf{v}_i^-(x, y) \\ &+ \sum_{i=0}^{N-2} -\sigma^{\text{te}} l_{N-1} \mathbf{v}_i^m(x, y) + \sigma^{\text{te}} \mathbf{v}_{N-1}^m(x, y) \end{aligned}$$

where for  $a \in [+,-,m]$ ,  $\mathbf{v}_i^a = \partial_{\bar{x}} \phi_i^a \mathbf{t}_i + \partial_{\bar{y}} \phi_i^a \mathbf{n}_i$

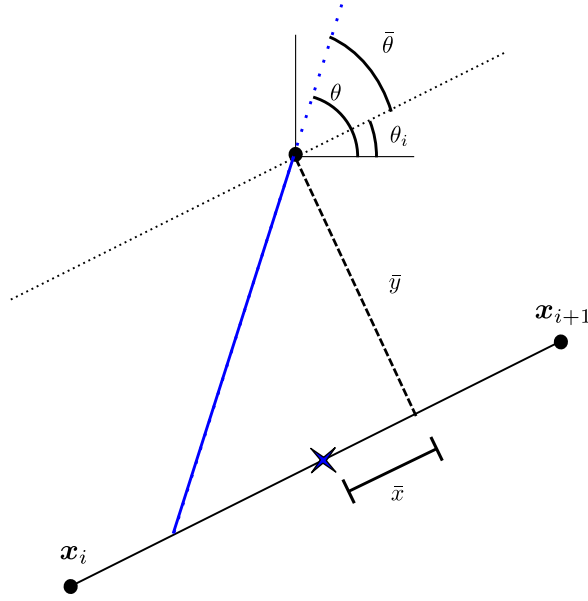


Fig. 13. Focus on a panel.

**Remark.** Integrals  $\phi_i^a$  have an analytical expression, these expressions are then derived against  $\bar{x}$  and  $\bar{y}$ . It is important to carry out the computation in that order as the inversion of derivation and integral is generally not allowed on a neighborhood of the section.

The velocity of the fluid is constrained by the impermeability condition on the section:  $\langle \mathbf{v}_1, \mathbf{n}_1 \rangle = 0$ . This expression is imposed on collocation points  $\mathbf{x}_i^c$  situated at the centers of each panels,  $N$  equations are determined, giving the matrix system of equations:

$$\mathbf{A}^v \boldsymbol{\gamma} + \sigma^{te} \mathbf{a}^m = \mathbf{N} \quad (60)$$

where  $v_{n,i,j}^a = \langle \mathbf{v}_j^a(x_i^c, y_i^c), \mathbf{n}_i \rangle$  for each  $a \in [+, -, m]$  and:

- $[\mathbf{A}^v]_{ij} = \frac{v_{n,i(j+1)}^+ + v_{n,i(j+1)}^-}{2} + \frac{v_{n,ij}^+ - v_{n,ij}^-}{2}$
- $[\mathbf{a}^m]_i = \sum_{j=0}^{N-2} -I_{N-1} v_{n,i,j}^m + v_{n,i(N-1)}^m$
- $[\mathbf{N}^m]_i = -v_\infty (\cos(\alpha) n_{i|x} + \sin(\alpha) n_{i|y})$

This system cannot be solved as it is of shape  $N \times (N + 1)$ , it is due to the fact that the circulation around a closed object is not determined in a perfect flow, the empirical Kutta condition (Katz and Plotkin, 2001) that reads:

$$\gamma_0 + \gamma_{N-1} = 0 \quad (61)$$

adds an equation and impose the value of the circulation, the equation becomes:

$$\begin{pmatrix} \mathbf{A}^v & \mathbf{a}^m \\ 1 & 0 & \dots & 0 & 1 & 0 \end{pmatrix} \begin{pmatrix} \gamma_0 \\ \vdots \\ \gamma_{N-1} \\ \sigma^{te} \end{pmatrix} = v_\infty \left( \cos(\alpha) \begin{pmatrix} n_{0|x} \\ \vdots \\ n_{N-1|x} \\ 0 \end{pmatrix} + \sin(\alpha) \begin{pmatrix} n_{0|y} \\ \vdots \\ n_{N-1|y} \\ 0 \end{pmatrix} \right) \quad (62)$$

## Appendix B. Propulsion structural problem discretization

### B.1. Internal stress power operator

The two following paragraphs made extensive use of Hoareau et al. (2022). The internal stress power operator is discretized on the initial configuration, rewritten on configuration  $C_0$  it reads:

$$W^{\text{int}}(\mathbf{u}_1, \mathbf{v}) = \int_{\Omega^s} J_{10}(\mathbf{X}) \boldsymbol{\sigma}_1(\mathbf{u}_1) : \boldsymbol{\epsilon}(\mathbf{v}) \quad (63)$$

where  $\epsilon(\boldsymbol{v}) = \frac{1}{2} (\nabla_1 \boldsymbol{v} + (\nabla_1 \boldsymbol{v})^T)$  is the virtual deformation tensor. The Cauchy tensor  $\boldsymbol{\sigma}_1$  and the Piola–Kirchhoff I tensor  $\boldsymbol{S}_1$  are linked by the expression:  $\boldsymbol{\sigma}_1 = J_{10}^{-1} \boldsymbol{F}_{10} \boldsymbol{S}_1 \boldsymbol{F}_{10}^T$ . Using  $\epsilon$  symmetry, the double contraction  $\boldsymbol{\sigma}_1 : \epsilon$  then reads:

$$J_{10} \boldsymbol{\sigma}_1 : \epsilon = \boldsymbol{S}_1 : (\boldsymbol{F}_{10}^T \epsilon \boldsymbol{F}_{10}) \quad (64)$$

The virtual deformation on configuration  $C_0$  is noted:  $\boldsymbol{E}^v = \boldsymbol{F}_{10}^T \epsilon \boldsymbol{F}_{10}$ , it can be rewritten with derivative on the initial configuration:

$$\boldsymbol{E}^v = \frac{1}{2} (\boldsymbol{F}_{10}^T \nabla_0 \boldsymbol{v} + (\nabla_0 \boldsymbol{v})^T \boldsymbol{F}_{10}) \quad (65)$$

The internal stress power operator then reads:

$$W^{\text{int}}(\boldsymbol{u}_1, \boldsymbol{v}) = \int_{\Omega^s} \boldsymbol{S}(\boldsymbol{u}_1) : \boldsymbol{E}^v(\boldsymbol{u}_1, \boldsymbol{v}) \quad (66)$$

The numerical procedure used to solve the nonlinear structure problem needs the differential of operator  $W^{\text{int}}$ . This expression can be computed by linearization of operator  $W^{\text{int}}(\boldsymbol{u}_1 + \delta \boldsymbol{u}, \boldsymbol{v})$  in  $\delta \boldsymbol{u}$ , its expression then reads:

$$dW_{\boldsymbol{u}_1}^{\text{int}}(\delta \boldsymbol{u}, \boldsymbol{v}) = \int_{\Omega^s} d\boldsymbol{S}_{\boldsymbol{u}_1}(\delta \boldsymbol{u}) : \boldsymbol{E}^v(\boldsymbol{u}_1, \boldsymbol{v}) + \boldsymbol{S}(\boldsymbol{u}_1) : d\boldsymbol{E}_{\boldsymbol{u}_1}^v(\delta \boldsymbol{u}, \boldsymbol{v}) \quad (67)$$

where  $d\boldsymbol{E}_{\boldsymbol{u}_1}^v(\delta \boldsymbol{u}, \boldsymbol{v}) = \frac{1}{2} ((\nabla_0 \delta \boldsymbol{u})^T \nabla_0 \boldsymbol{v} + (\nabla_0 \boldsymbol{v})^T \nabla_0 \delta \boldsymbol{u})$ . These operators are then discretized using the finite element method, the internal stress operators then reads:

$$W^{\text{int}}(\boldsymbol{u}_1, \boldsymbol{v}) \Rightarrow \langle \boldsymbol{F}^{\text{int}}(\boldsymbol{U}_1), \boldsymbol{V} \rangle \quad (68)$$

and the differential operator reads:

$$dW_{\boldsymbol{u}_1}^{\text{int}}(\delta \boldsymbol{u}, \boldsymbol{v}) \Rightarrow \langle \boldsymbol{K}^{\text{int}}(\boldsymbol{U}_1) \delta \boldsymbol{U}, \boldsymbol{V} \rangle \quad (69)$$

where  $\boldsymbol{U}_1$ ,  $\delta \boldsymbol{U}$  and  $\boldsymbol{V}$  are displacement nodal vectors,  $\boldsymbol{F}^{\text{int}}(\boldsymbol{U}_1)$  is the internal stress nodal force vector and  $\boldsymbol{K}^{\text{int}}(\boldsymbol{U}_1)$  is the internal forces contribution to the tangential rigidity matrix

### B.2. External stress power operator

The following pressure field  $p$  is taken into account by external stress operator  $W^{\text{ext}}(\boldsymbol{u}_1, \boldsymbol{v})$ , it is nonlinear in  $\boldsymbol{u}_1$  because the normal vector  $\boldsymbol{n}_1$  depends on the geometry. The differential of  $W^{\text{ext}}(\boldsymbol{u}_1, \boldsymbol{v})$  can be computed by linearization of  $W^{\text{ext}}(\boldsymbol{u}_1 + \delta \boldsymbol{u}, \boldsymbol{v})$ ,

$$dW_{\boldsymbol{u}_1}^{\text{ext}}(\delta \boldsymbol{u}, \boldsymbol{v}) = \int_{\partial \Omega^s} p_1 \langle d\boldsymbol{n}_{\boldsymbol{u}_1}(\delta \boldsymbol{u}), \boldsymbol{v} \rangle \quad (70)$$

The external stress operator  $W^{\text{ext}}$  and its differential  $dW^{\text{ext}}$  are discretized using the finite element method, their expression does not need to be rewritten on the initial configuration  $C_0$  as each surface element on configuration  $C_1$  can be parameterized using the reference element in a straightforward manner. The discretized external stress operator reads:

$$W^{\text{ext}}(\boldsymbol{u}_1, \boldsymbol{v}) \Rightarrow \langle \boldsymbol{F}^{\text{ext}}(\boldsymbol{U}_1), \boldsymbol{V} \rangle \quad (71)$$

and the discretized differential reads:

$$dW_{\boldsymbol{u}_1}^{\text{ext}}(\delta \boldsymbol{u}, \boldsymbol{v}) \Rightarrow \langle \boldsymbol{K}^{\text{ext}}(\boldsymbol{U}_1) \delta \boldsymbol{U}, \boldsymbol{V} \rangle \quad (72)$$

Vector  $\boldsymbol{F}^{\text{ext}}(\boldsymbol{U}_1)$  is the external stress nodal force vector and  $\boldsymbol{K}^{\text{ext}}(\boldsymbol{U}_1)$  is the external forces contribution to the tangential rigidity matrix

### B.3. Gyroscopic operator

The gyroscopic operator can be split into two contributions:

- A linear form that takes into account the rigid body centrifugal forces:

$$W_r^g(\boldsymbol{v}) = \int_{\Omega^s} \rho^s (\omega_p \boldsymbol{R})^2 \langle \boldsymbol{X}, \boldsymbol{v} \rangle \quad (73)$$

- A bilinear form that takes into account the deformation of the structure

$$W_d^g(\boldsymbol{u}_1, \boldsymbol{v}) = \int_{\Omega^s} \rho^s (\omega_p \boldsymbol{R})^2 \langle \boldsymbol{u}_1, \boldsymbol{v} \rangle \quad (74)$$

These operator are also discretized using the finite element method:

$$W_r^g(\boldsymbol{v}) \Rightarrow \langle \boldsymbol{F}^r, \boldsymbol{V} \rangle \quad (75)$$

and

$$W_d^g(\boldsymbol{u}_1, \boldsymbol{v}) \Rightarrow \langle \boldsymbol{N} \boldsymbol{U}_1, \boldsymbol{V} \rangle \quad (76)$$

## References

- Amestoy, P., Duff, I., L'Excellent, J.-Y., Koster, J., 2002. Multifrontal Massively Parallel Solver (MUMPS Version 4.2 Beta) User's Guide. Research Report LIP TR-2002-02, Laboratoire de l'informatique du parallélisme, p. 2+28p.
- Bayliss, A., Gunzburger, M., Turkel, E., 1982. Boundary conditions for the numerical solution of elliptic equations in exterior regions. *SIAM J. Appl. Math.* 42 (2), 430–451. <http://dx.doi.org/10.1137/0142032>.
- Behnel, S., Bradshaw, R., Citro, C., Dalcin, L., Seljebotn, D., Smith, K., 2011. Cython: The best of both worlds. *Comput. Sci. Eng.* 13, 31–39. <http://dx.doi.org/10.1109/MCSE.2010.118>.
- Boncoraglio, G., Farhat, C., Bou-Mosleh, C., 2021. Model reduction framework with a new take on active subspaces for optimization problems with linearized fluid-structure interaction constraints. *Internat. J. Numer. Methods Engrg.* 122 (19), 5450–5481. <http://dx.doi.org/10.1002/nme.6376>.
- Chandra, R., Dagum, L., Kohr, D., Menon, R., Maydan, D., McDonald, J., 2001. *Parallel Programming in OpenMP*. Morgan Kaufmann.
- Choi, Y.-S., Joe, B.-J., Jang, W.-S., Hong, S.-Y., Song, J.-H., Kwon, H.-W., 2022. Numerical investigation of BPF noise for flexible submarine propeller design including inertial force coupling. *J. Mar. Sci. Technol.* 27 (1), 648–664. <http://dx.doi.org/10.1007/s00773-021-00859-1>.
- Drela, M., 1989. XFOIL: An Analysis and Design System for Low Reynolds Number Airfoils. Vol. 54, [http://dx.doi.org/10.1007/978-3-642-84010-4\\_1](http://dx.doi.org/10.1007/978-3-642-84010-4_1).
- EDF, 1989. Finite element code\_aster, analysis of structures and thermomechanics for studies and research.
- Everstine, G.C., 1981. A symmetric potential formulation for fluid-structure interaction. *J. Sound Vib.* 79 (1), 157–160.
- George, S., Ducoin, A., 2021. A coupled direct numerical simulation of IDOF vibration approach to investigate the transition induced vibration over a hydrofoil. *J. Fluids Struct.* 105, 103345. <http://dx.doi.org/10.1016/j.jfluidstructs.2021.103345>.
- Glauert, H., 1935. *Airplane propellers*. In: Durand, W. (Ed.), *Aerodynamic Theory*. Vol. IV, Division L, Springer, New York, pp. 169–360.
- Goody, M., 2004. Empirical spectral model of surface pressure fluctuations. *AIAA J.* 42 (9), 1788–1794. <http://dx.doi.org/10.2514/1.9433>.
- Harris, C.R., Millman, K.J., van der Walt, S.J., Gommers, R., Virtanen, P., Cournapeau, D., Wieser, E., Taylor, J., Berg, S., Smith, N.J., Kern, R., Picus, M., Hoyer, S., van Kerkwijk, M.H., Brett, M., Haldane, A., del Río, J.F., Wiebe, M., Peterson, P., Gérard-Marchant, P., Sheppard, K., Reddy, T., Weckesser, W., Abbasi, H., Gohlke, C., Oliphant, T.E., 2020. Array programm. *NumPy*. *Nature* 585 (7825), 357–362. <http://dx.doi.org/10.1038/s41586-020-2649-2>.
- Hirt, C.W., Amsden, A.A., Cook, J.L., 1974. An arbitrary Lagrangian-Eulerian computing method for all flow speeds. *J. Comput. Phys.* 14 (3), 227–253. [http://dx.doi.org/10.1016/0021-9991\(74\)90051-5](http://dx.doi.org/10.1016/0021-9991(74)90051-5).
- Hoareau, C., Deü, J.-F., Ohayon, R., 2022. Hydroelastic linearized vibrations taking into account prestressed effects due to internal liquid weight: Numerical vs. Experimental results. *J. Fluids Struct.* 112, 103596. <http://dx.doi.org/10.1016/j.jfluidstructs.2022.103596>.
- Kalumuck, K.M., Duraiswami, R., Chahine, G.L., 1995. Bubble dynamics fluid-structure interaction simulation by coupling fluid bem and structural fem codes. *J. Fluids Struct.* 9 (8), 861–883. <http://dx.doi.org/10.1006/jfls.1995.1049>.
- Katz, J., Plotkin, A., 2001. *Low Speed Aerodynamics*. Cambridge University press.
- Kim, J.-H., Ahn, B.-K., Ruy, W., Kim, G.-D., Lee, C.-S., 2021. Fluid-Structure Interaction Analysis of Flexible Composite Propellers. pp. 519–538. [http://dx.doi.org/10.1007/978-981-15-4624-2\\_31](http://dx.doi.org/10.1007/978-981-15-4624-2_31).
- Kim, K.-H., Bang, J.-S., Kim, J.-H., Kim, Y., Kim, S.-J., Kim, Y., 2013. Fully coupled BEM-FEM analysis for ship hydroelasticity in waves. *Mar. Struct.* 33, 71–99. <http://dx.doi.org/10.1016/j.marstruc.2013.04.004>.
- Leblond, C., 2022. “Advanced” methods for the vibro-acoustic response of naval structures. In: *Fluid –Structure Interaction*. John Wiley & Sons, Ltd, pp. 79–111. <http://dx.doi.org/10.1002/9781394188222.ch4>.
- Leblond, C., Sigrist, J.-F., 2016. A reduced basis approach for the parametric low frequency response of submerged viscoelastic structures. *Finite Elem. Anal. Des.* 119, 15–29. <http://dx.doi.org/10.1016/j.finela.2016.05.002>.
- Lin, H.-J., Lin, J.-J., 1996. Nonlinear hydroelastic behavior of propellers using a finite-element method and lifting surface theory. *J. Mar. Sci. Technol.* 1 (2), 114–124. <http://dx.doi.org/10.1007/BF02391167>.
- Maday, Y., Stamm, B., 2013. Locally adaptive greedy approximations for anisotropic parameter reduced basis spaces. *SIAM J. Sci. Comput.* 35 (6), A2417–A2441. <http://dx.doi.org/10.1137/120873868>.
- Meyer, V., Maxit, L., 2022. Hybrid methods for the vibro-acoustic response of submerged structures. In: *Fluid –Structure Interaction*. John Wiley & Sons, Ltd, pp. 53–78. <http://dx.doi.org/10.1002/9781394188222.ch3>.
- Morand, H.J.-P., Ohayon, R., 1995. *Fluid-Structure Interaction*, John Wiley & Sons.
- Muller, P., Pécot, F., 2017. Development of a fluid structure coupling for composite tidal turbines and marine propellers.
- Pernod, L., Ducoin, A., Sourne, H., Sigrist, J.-F., 2017. Coupled Numerical Simulation of an Aluminum and a Composite Hydrofoil in Steady and Unsteady Flows. Rakotomalala, Q., Leblond, C., Dolo, G., Deu, J.-F., Rouleau, L., Ducoin, A., 2024. Iterative fluid-structure resolution, correlation on a simplified composite blade tested in a traction canal. In: *16eme Colloque National En Calcul Des Structures*. Giens (Var), France.
- Rouleau, L., Deü, J.-F., Legay, A., Sigrist, J.-F., 2012. Vibro-acoustic study of a viscoelastic sandwich ring immersed in water. *J. Sound Vib.* 331(3), 522–539. <http://dx.doi.org/10.1016/j.jsv.2011.10.004>.
- Rouleau, L., Legay, A., Deü, J.-F., 2018. Interface finite elements for the modelling of constrained viscoelastic layers. *Compos. Struct.* 204, <http://dx.doi.org/10.1016/j.compstruct.2018.07.126>.
- Sigrist, J.-F., 2015. *Fluid-Structure Interaction: An Introduction to Finite Element Coupling*.
- Sigrist, J.-F., 2022. Numerical methods for vibro-acoustics of ships in the “Low frequency” range. In: *Fluid –Structure Interaction*. John Wiley & Sons, Ltd, pp. 31–51. <http://dx.doi.org/10.1002/9781394188222.ch2>.
- Smith, T.A., Rigby, J., 2022. Underwater radiated noise from marine vessels: A review of noise reduction methods and technology. *Ocean Eng.* 266, 112863. <http://dx.doi.org/10.1016/j.oceaneng.2022.112863>.
- Taketani, T., Kimura, K., Ando, S., Yamamoto, K., 2013. Study on Performance of a Ship Propeller Using a Composite Material. In: *Third International Symposium on Marine Propulsors*, Launceston, Tasmania, Australia.
- Testa, C., Ianniello, S., Salvatore, F., 2018. A fowcs williams and hawkins formulation for hydroacoustic analysis of propeller sheet cavitation. *J. Sound Vib.* 413, 421–441. <http://dx.doi.org/10.1016/j.jsv.2017.10.004>.
- Van Rossum, G., Drake, F.L., 2009. *Python 3 Reference Manual*. CreateSpace, Scotts Valley, CA.
- Wilcox, D.C., 2008. Formulation of the K-w turbulence model revisited. *AIAA J.* 46 (11), 2823–2838. <http://dx.doi.org/10.2514/1.36541>.
- Young, Y.L., 2008. Fluid – structure interaction analysis of flexible composite marine propellers. *J. Fluids Struct.* 24, 799–818. <http://dx.doi.org/10.1016/j.jfluidstructs.2007.12.010>.